Germ fate determinants protect germ precursor cell division by reducing septin and anillin levels at the cell division plane

Caroline Q. Connors[a,†], Michael S. Mauro[a,†], J. Tristian Wiles[b], Andrew D. Countryman[c], Sophia L. Martin[a], Benjamin Lacroix[d,e], Mimi Shirasu-Hiza[f], Julien Dumont[d], Karen E. Kasza[g], Timothy R. Davies[a,h], and Julie C. Canman[a,*]

[a]Department of Pathology and Cell Biology, and [f]Department of Genetics and Development, Columbia University Irving Medical Center, New York, NY 10032; [b]Department of Biological Sciences, [c]Department of Biomedical Engineering, and [g]Department of Mechanical Engineering, Columbia University, New York, NY 10027; [d]Université Paris Cité, CNRS, Institut Jacques Monod, F-75013 Paris, France; [e]Université de Montpellier, CNRS, Centre de Recherche en Biologie Cellulaire de Montpellier, UMR 5237 Montpellier, France; [h]Department of Biosciences, Durham University, Durham DH1 3LE, UK

ABSTRACT **Animal cell cytokinesis, or the physical division of one cell into two, is thought to be driven by constriction of an actomyosin contractile ring at the division plane. The mechanisms underlying cell type-specific differences in cytokinesis remain unknown. Germ cells are totipotent cells that pass genetic information to the next generation. Previously, using *formin*$^{cyk\text{-}1}$*(ts)* mutant *Caenorhabditis elegans* 4-cell embryos, we found that the P2 germ precursor cell is protected from cytokinesis failure and can divide with greatly reduced F-actin levels at the cell division plane. Here, we identified two canonical germ fate determinants required for P2-specific cytokinetic protection: PIE-1 and POS-1. Neither has been implicated previously in cytokinesis. These germ fate determinants protect P2 cytokinesis by reducing the accumulation of septin$^{UNC\text{-}59}$ and anillin$^{ANI\text{-}1}$ at the division plane, which here act as negative regulators of cytokinesis. These findings may provide insight into the regulation of cytokinesis in other cell types, especially in stem cells with high potency.**

SIGNIFICANCE STATEMENT

- In 4-cell worm embryos, cell division in the P2 germ precursor cell is uniquely protected against severe perturbations of the actin cytoskeleton. The mechanisms that underly this cell type-specific protection of cell division remain unclear.
- We identified two well-known germ fate determinants as required for cell type-specific protection of P2 cell division when actin levels are reduced. We show these germ fate determinants protect cell division by controlling the levels of specific contractile ring-associated proteins to ensure cell division completes successfully.
- These results suggest that cell type-specific protection of germ precursor cell division is inextricably linked to its cellular identity.

Monitoring Editor
William Bement
University of Wisconsin, Madison

Received: Mar 8, 2024
Revised: Apr 22, 2024
Accepted: Apr 26, 2024

INTRODUCTION

Germ cells play a unique role in passing genetic information from one generation to the next. Perhaps because germ cell integrity is critical for fitness and continuation of the species, there appear to be specific mechanisms to protect germ cell fate, survival, and proliferation. For example, germ precursor cells undergo specific differential developmental pathways (Foe, 1989; Lehmann and Ephrussi, 1994; Strome, 2005; Strome and Lehmann, 2007; Saga, 2008; Saitou, 2009; Wang and Seydoux, 2013; Wessel *et al.*, 2014; Strome and Updike, 2015; Roelen and Chuva de Sousa Lopes, 2022). There is also evidence in several model systems that cytokinesis in germ precursor cells is differentially regulated from in somatic cells. Cytokinesis is the physical division of one cell into two, which occurs at the end of the cell cycle. In many metazoan germ cells, unlike in somatic cell divisions (Andrade and Echard, 2022), daughter cells are not severed via abscission and remain connected by a stable intercellular bridge (for review, see Gerhold *et al.*, 2022). In *Drosophila*, mutations in the cytoskeletal interacting protein anillin specifically affect somatic cell but not germ precursor cell cellularization (Adam *et al.*, 2000; Field *et al.*, 2005). In our own previous work, we found that cytokinesis in *Caenorhabditis elegans* germ precursor cells is uniquely resistant to severe perturbations of the actin cytoskeleton that completely block cytokinesis in somatic cells (Davies *et al.*, 2018) (see also Bauer *et al.*, 2021). Thus, cell division in germ precursor cells appears to have significant differences in regulation from somatic precursor cell division.

These data contradict the textbook view of cytokinesis that all animal cells divide using the same molecular machinery. It is thought that anaphase onset drives mitotic spindle signaling to promote the assembly and constriction of an actomyosin contractile ring at the cell division plane to power cytokinesis. In fact, growing evidence supports both cell type-specific regulation of cytokinesis and cell type-specific consequences for cytokinesis failure. Animals from worms to humans can have organism-wide genetic mutations that result in highly cell type-specific cytokinetic consequences (Bione *et al.*, 1998; Di Cunto *et al.*, 2000; LoTurco *et al.*, 2003; Paw *et al.*, 2003; Morita *et al.*, 2005; Ackman *et al.*, 2007; Moulding *et al.*, 2007; Muzzi *et al.*, 2009; Vinciguerra *et al.*, 2010; Jackson *et al.*, 2011; Liljeholm *et al.*, 2013; Menon *et al.*, 2014; Taniguchi *et al.*, 2014; Basit *et al.*, 2016; Harding *et al.*, 2016; Li *et al.*, 2016; Sgro *et al.*, 2016; Shaheen *et al.*, 2016; Davies *et al.*, 2018; Wontakal *et al.*, 2022). On one hand, cell type-specific failure in cytokinesis, resulting in a binucleated tetraploid cell, is emerging as an important contributor to many diseases including blood disorders, neurological diseases, and cancer (Bione *et al.*, 1998; Ganem *et al.*, 2007; Moulding *et al.*, 2007; Dieterich *et al.*, 2009; Vinciguerra *et al.*, 2010; Lacroix and Maddox, 2012; Iolascon *et al.*, 2013; Liljeholm *et al.*, 2013; Ferrer *et al.*, 2014; Ganem *et al.*, 2014; Tormos *et al.*, 2015; Seu *et al.*, 2020; Wontakal *et al.*, 2022). On the other hand, cytokinesis failure is not always pathogenic and specific cell types (e.g., hepatocytes in the liver and intermediate cells in the bladder) are naturally programmed to fail in cytokinesis and become binucleated (or multinucleated) as a normal part of human development and tissue homeostasis (Li *et al.*, 1997; Ravid *et al.*, 2002; Li, 2007; Margall-Ducos *et al.*, 2007; Lacroix and Maddox, 2012; Takegahara *et al.*, 2016; Wang *et al.*, 2018; Sladky *et al.*, 2021). Despite this strong supporting evidence of cell type-specific regulation of cytokinesis, the molecular mechanisms remain poorly understood.

In theory, the molecular mechanisms differentially regulating cytokinesis in different cell types should arise in the literature as molecules that differentially affect cell division in different cell types and model systems. Two such candidates for cell type-specific regulation of cytokinesis are the septins and anillin. Septins and anillin are cytoskeletal-binding proteins essential for cytokinesis in some, but not all, cell types and model systems; their precise roles in cytokinesis remain unclear (Piekny and Maddox, 2010; Menon and Gaestel, 2015; Woods and Gladfelter, 2021). The septins are essential for cytokinesis in budding yeast (Fares *et al.*, 1996; Mela and Momany, 2019) but are not required for cytokinesis in other cell types, including in *Schizosaccharomyces pombe* (Longtine *et al.*, 1996), mouse myeloid and lymphoid hematopoietic cells (Menon *et al.*, 2014), and mouse neuronal precursor cells (Qiu *et al.*, 2020). And, in cultured mammary epithelial cells, *septin-6* expression is inversely correlated with successful cytokinesis, suggesting an inhibitory role (Rabie *et al.*, 2021). Similarly, anillin is required for cytokinesis in some cell types (Giansanti *et al.*, 1999; Oegema *et al.*, 2000; Straight *et al.*, 2005), including in the fission yeast *S. pombe* (Hachet and Simanis, 2008; Rincon and Paoletti, 2012; Saha and Pollard, 2012), *Drosophila* S2 cells (Straight *et al.*, 2005; Kechad *et al.*, 2012), and HeLa cells (Straight *et al.*, 2005), but not required in many cell types, including the fission yeast *Schizosaccharomyces japonicus* (Gu *et al.*, 2015). In *Saccharomyces cerevisiae*, anillin (Boi1/2p) is only required for cytokinesis in the presence of DNA bridges in the cell division plane (Norden *et al.*, 2006; Masgrau *et al.*, 2017). In *C. elegans*, neither the septins (UNC-59/-61) nor anillin (ANI-1) are required for early cleavage divisions during embryogenesis (Nguyen *et al.*, 2000; Maddox *et al.*, 2007). Even in one-celled organisms that require septins and anillin, these proteins have different functions and localization than in multicellular organisms. For example, the septin ring at the bud neck in *S. cerevisiae* splits into two rings that sandwich, rather than overlap with, the actomyosin contractile ring prior to ring constriction (Tamborrini and Piatti, 2019; Marquardt *et al.*, 2021). Moreover, this

This article was published online ahead of print in MBoC in Press (http://www.molbiolcell.org/cgi/doi/10.1091/mbc.E24-02-0096-T) on May 2, 2024.

†These authors contributed as co-first authors to this work.

Author contributions: C.Q.C., T.R.D., M.S.M, J.T.W., and J.C.C. conceived of the project and designed all experiments. C.Q.C., J.T.W., and T.D. did the mini-RNAi screen to identify genes required for P2 cytokinesis in *formin(ts)* embryos. M.S.M. did all injections for injection-based RNAi depletion (except four replicates in the PIE-1 and POS-1 RNAi validation, which were done by J.T.W.) and performed all quantitative imaging and analysis of contractile ring protein levels. C.Q.C. did all imaging and analysis of cytokinesis outcome experiments, contact angles, central spindle assembly kinetics, and imaging of PIE-1, POS-1, and UNC-59 levels with and without double RNAi (analysis done by M.S.M.), except for cytokinesis outcome analysis upon CCCH Zn-finger depletion in control embryos, which was done by S.L.M., or in *formin(ts)* embryos without RNAi or with *ani-1(RNAi)*, which was done by J.T.W.. J.T.W. imaged and quantified CCCH Zn-finger protein levels with and without RNAi in controls and performed P2 spindle, daughter cell size, and MT growth rate imaging and analysis. A.D.C. and K.E.K. did the cell tension data analysis. C.Q.C., M.S.M., J.T.W., A.D.C., K.E.K., B.L., M.S.-H., J.D., and T.R.D., and J.C.C. made intellectual contributions and helped write (or edit) the manuscript. C.Q.C., M.S.M., J.T.W., A.D.C., and J.C.C. made the figures.

Conflicts of interests: The authors declare no financial conflict of interest.

*Address correspondence to: Julie C. Canman (jcc2210@columbia.edu).

Abbreviations used: ANI-1, anillin; DIC, differential interference contrast; dsRNA, double stranded ribonucleic acid; EB1, end binding 1; EBP-2, microtubule end binding protein-2; F-actin, filamentous actin; *formin(ts)*, *cyk-1(or596ts)*; GFP, green fluorescent protein; H2B, histone H2B; HDA-1, histone deacetylase-1; MEX-1, muscle excess-1; NMY-2, non-muscle myosin-2; NuRD, nucleosome remodeling deacetylase; PH, pleckstrin homology; PIE-1, pharynx and intestine in excess-1; PLST-1, plastin homolog-1; POS-1, posterior segregation-1; RFP, red fluorescent protein; RNAi, RNA interference; SUMO, small ubiquitin-like modifier; ts, temperature sensitive; UNC-59/-61, uncoordinated-59/-61 (worm septins); UTR, untranslated region; Zn-finger, Zinc-finger.

splitting of septins is required for cytokinesis to proceed, again suggesting septins may act as negative regulators of ring constriction (Tamborrini *et al.*, 2018; Tamborrini and Piatti, 2019). Likewise, in *S. pombe*, anillin (Mid1p) leaves the division plane before contractile ring constriction (Wu *et al.*, 2003). These data suggest a cell type- and model system-specific role for septins and anillin in cytokinesis.

We hypothesize that septins and anillin play a key role in cell type-specific differences in cytokinesis, particularly in protection of cytokinesis in the germ lineage when F-actin levels are reduced. In previous work, we found that septin^{UNC-59} and anillin^{ANI-1} likely act as negative regulators of mitotic cytokinesis in 1-cell *C. elegans* embryos (Jordan *et al.*, 2016). We also identified cell type-specific regulation of cytokinesis at the 4- to 8-cell stage for the germ precursor cell. We weakened the actin cytoskeleton using either a genetically encoded fast-acting temperature sensitive (ts) mutant that affects the filamentous actin (F-actin) nucleating activity (Davies *et al.*, 2014) of the diaphanous family formin^{CYK-1} (hereafter, *formin(ts)*), or a chemical inhibitor of F-actin assembly, Latrunculin A. Under both conditions, the two anterior cells (ABa and ABp) always failed in cytokinesis, whereas the two posterior cells (EMS and P2) divided successfully at a high frequency, even without detectable F-actin in the cell division plane (Davies *et al.*, 2018). Interestingly, we found that cytokinetic protection of EMS and P2 is regulated by a distinct molecular mechanism in each cell. Using embryo microdissection to physically separate each of the 4 cells from *formin(ts)* embryos, only the P2 germ precursor cell was still protected from cytokinesis failure; EMS lost its protection and failed to divide (Davies *et al.*, 2018). Thus, cell type-specific protection of cytokinesis in the P2 germ precursor cell is cell-intrinsic and in the EMS cell it is cell-extrinsic.

Here, to examine the cell type-specific regulation of cytokinesis that underlies cell-intrinsic protection of germ precursor cells, we examined the role of germ cell fate determinants in cytokinesis. Three well-established and essential germ cell fate determinants are MEX-1, PIE-1, and POS-1, all of which encode CCCH Zn-finger proteins (Mello *et al.*, 1996; Guedes and Priess, 1997; Tabara *et al.*, 1999). PIE-1 (pharynx and intestine in excess) is a master regulator of germ cell fate specification in worms (Mello *et al.*, 1992; Mango *et al.*, 1994; Bowerman, 1995; Mello *et al.*, 1996; Strome, 2005). PIE-1 is asymmetrically inherited by the germ precursor cells where it localizes to ribonucleoprotein condensates called germ granules (or P granules) and to the nucleus during interphase, but during mitosis it relocalizes to the centrosomes (Mello *et al.*, 1996; Tenenhaus *et al.*, 1998; Reese *et al.*, 2000). Several other CCCH Zn-finger proteins, including POS-1 and MEX-1, cooperate to control proper PIE-1 localization in germ precursor cells (Guedes and Priess, 1997; Tabara *et al.*, 1999; Tenenhaus *et al.*, 2001) and residual PIE-1 protein (and POS-1 and MEX-1) in somatic daughters is degraded via proteolysis in an E3 ligase substrate adaptor (ZIF-1)-dependent manner (DeRenzo *et al.*, 2003; Oldenbroek *et al.*, 2012). PIE-1 canonically controls germ fate specification by regulating transcription (Seydoux *et al.*, 1996; Seydoux and Dunn, 1997; Batchelder *et al.*, 1999; Zhang *et al.*, 2003; Ghosh and Seydoux, 2008), gene silencing (Kim *et al.*, 2021), translation (Tenenhaus *et al.*, 2001), and posttranslational modifications (e.g., acetylation and SUMOylation) (Kim *et al.*, 2021) through inhibition of a NuRD (nucleosome remodeling and deacetylase) complex (Unhavaithaya *et al.*, 2002). Neither PIE-1, nor other CCCH Zn-finger proteins that regulate germ fate in *C. elegans*, have previously been implicated in cytokinesis.

We show that protection of P2 cytokinesis is tied to its cellular identity as a germline precursor cell. While another group recently reported a positive role for anillin^{ANI-1} during cytokinesis when central spindle assembly is disrupted in the EMS cell at the 4-cell stage (Santos *et al.*, 2023), our research aligns more closely with instances in numerous animal cell types in which septins and anillin are present at the division plane but are not required for cytokinesis. Here we provide evidence that septins and anillin not only act as negative regulators of cytokinesis but also are controlled by germ cell fate determinants that promote cytokinetic protection. The totipotent P2 germ precursor cell is required to produce all gametes (oocytes and sperm) in the adult worm (Sulston *et al.*, 1983). We identify three germ fate determinants required for protection of P2 cytokinesis in *formin(ts)* embryos. Depletion of either MEX-1, PIE-1, or POS-1 led to loss of cytokinetic protection and P2 cytokinesis failure in *formin(ts)* embryos, but not in control embryos. Depletion of MEX-1 also led to EMS cytokinesis failure, whereas PIE-1 and POS-1 acted in a P2 cell-specific way. We found that PIE-1 does not appear to play a major role in controlling many factors known to affect cytokinesis, including cell surface tension, spindle dynamics, and asymmetric cell division. Instead, our analysis revealed that these germ fate determinants protect cytokinesis by blocking the excessive accumulation of both septin^{UNC-59} and its binding partner, anillin^{ANI-1}, at the P2 cell division plane. Codepletion of septin^{UNC-59} and PIE-1 (or POS-1) was necessary and sufficient to both reduce anillin^{ANI-1} levels at the P2 division plane and restore cytokinetic protection of P2 in *formin(ts)* embryos. Thus, germ fate specification promotes robust cytokinesis in the P2 germ precursor cell, even when F-actin levels are greatly reduced, at least in part by reducing the levels of septin^{UNC-59} and anillin^{ANI-1} at the P2 division plane.

RESULTS

Protection of P2 cytokinesis requires the germ cell fate determinants MEX-1, POS-1, and PIE-1

To identify genes required to protect the P2 germ precursor cell (Figure 1A) against cytokinesis failure when the actin cytoskeleton is weakened, we performed a targeted mini-screen of candidate genes either implicated in germ fate regulation in the literature or differentially expressed in the P2 cell by single-cell transcriptomics (Tintori *et al.*, 2016). Embryonic lethality at permissive temperature was used as a proxy for effective gene knockdown (when applicable, see Supplemental Figure S1B). To weaken the actin cytoskeleton, we used the temperature sensitive *formin^{cyk-1}(or596ts)* mutant (*formin(ts)*), which completely blocks cytokinesis in the 1-cell embryo at restrictive temperature with little to no contractile ring constriction or detectable F-actin in the division plane (Davies *et al.*, 2014; Davies *et al.*, 2018). P2 cytokinesis was monitored by time-lapse spinning disk confocal microscopy in embryos expressing fluorescently-tagged reporters for the plasma membrane and chromatin (GFP::PH$^{PLC\delta}$ and mCherry::histone H2B^{HIS-58}, respectively [Audhya *et al.*, 2005]; Figure 1B). *Control* (empty vector) and candidate feeding RNA-mediated interference (RNAi)-treated *formin(ts)* 4-cell embryos were upshifted from 16°C (permissive temperature) to ~24.5–25.5°C (semirestrictive temperature) prior to anaphase onset in the P2 cell (Figure 1, B and C). In untreated *formin(ts)* control embryos at this temperature, while ABa and ABp were unable to divide (0% cytokinesis completion), many EMS and P2 cells completed cytokinesis successfully (68% EMS and 50% P2 cytokinesis completion, respectively; Supplemental Figure S1A). The P2 cell in *control* RNAi-treated embryos also frequently completed cytokinesis successfully (78% P2 cytokinesis completion, Figure 1C). While RNAi of most candidate genes did not block P2 cytokinesis, we identified three genes required for P2 cytokinesis in *formin(ts)* embryos. Specifically, RNAi-mediated knockdown of MEX-1, PIE-1, and POS-1 significantly decreased the rate of cytokinesis completion in *formin(ts)* P2 cells (28%, 15%, and 27% cytokinesis completion, respectively;

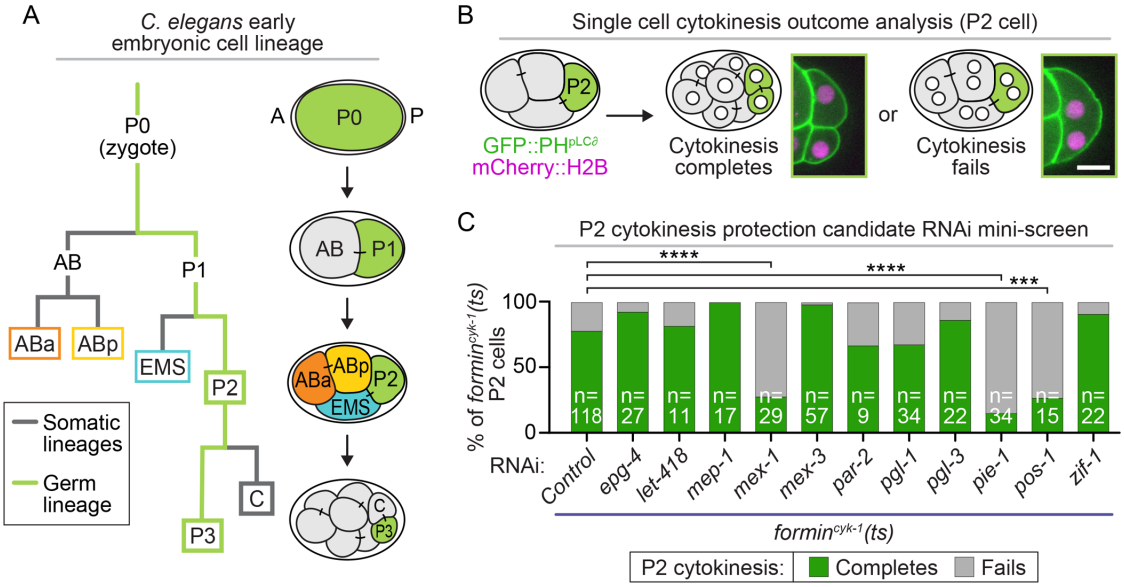

FIGURE 1: RNAi-based mini-screen of candidate genes required for protection of P2 cytokinesis in formin$^{cyk\text{-}1}$(ts) embryos. (A) Schematic of *C. elegans* early embryonic cell lineage map from the 1- to 4-cell stage (8-cell stage for germ lineage); A = anterior of embryo; P = posterior of embryo; gray lines = somatic cell lineages, lime green lines = germ lineage. (B) Schematic of single-cell cytokinesis outcome analysis for the P2 cell. Representative single plane images show the result of P2 cytokinesis completion (left, 2 mononucleated daughter cells) or failure (right, 1 binucleated daughter cell) in *formin$^{cyk\text{-}1}$(ts)* embryos expressing GFP::PH$^{PLC\delta}$ (green, plasma membrane) and mCherry::histone H2B$^{HIS\text{-}58}$ (magenta, chromatin); scale bar = 10 µm. (C) Graph showing the percentage of P2 cells in *formin$^{cyk\text{-}1}$(ts)* embryos that complete (green) or fail (gray) in cytokinesis with or without feeding RNAi treatment; *n* = number of P2 cells scored and is indicated on each bar; ***, *P*-value ≤ 0.001; ****, *P*-value ≤ 0.0001 (Fisher's exact test; see also Supplemental Table S1).

Figure 1C). These proteins are all CCCH Zn-finger family members essential for proper germ fate specification but not previously implicated in cytokinesis. This result suggests that cytokinetic protection of P2 depends on the germ fate determinants MEX-1, PIE-1, and POS-1.

We next sought to determine whether this CCCH Zn-finger family-mediated protection of P2 cytokinesis is cell type specific. We upshifted 4- to 8-cell control and *formin(ts)* embryos prior to anaphase onset in each of the individual 4 cells with and without MEX-1, PIE-1, or POS-1 RNAi-treatment and monitored cytokinesis, as above. For these experiments (and hereafter), we switched to injection RNAi, which is more robust than feeding RNAi in our hands. RNAi knockdown was confirmed by both loss of fluorescent signal in 4-cell embryos expressing fluorescently-tagged reporters of these CCCH Zn-finger proteins (<1%, 4.7%, and <1% of control levels of GFP::MEX-1 [Wu *et al.*, 2015], GFP::PIE-1 [Merritt *et al.*, 2008], and POS-1::GFP [Tsukamoto *et al.*, 2017], respectively; Supplemental Figure S2, A–D) and consistently high (>99%) embryonic lethality (Supplemental Figure S2, E–G). In control embryos, RNAi-mediated knockdown of MEX-1, PIE-1, or POS-1 did not affect cytokinesis in any cell of the 4 cells (100% cytokinesis completion; Figure 2A), as predicted (Mello *et al.*, 1992; Tabara *et al.*, 1999). In *formin(ts)* embryos, knockdown of MEX-1, PIE-1, or POS-1 did not change the high rate of cytokinesis failure in the ABa or ABp cells (0% cytokinesis completion in both ABa and ABp; Figure 2B) but led to a high frequency of P2 cytokinesis failure (0%–8% cytokinesis completion; Figure 2, B and C). RNAi knockdown of MEX-1, but not PIE-1 or POS-1, also led to a high frequency of EMS cytokinesis failure in *formin(ts)* embryos (0% EMS cytokinesis completion in *mex-1(RNAi)*; Figure 2B). Together, these results suggest that PIE-1 and POS-1 provide cell type-specific cytokinetic protection of P2, whereas MEX-1 protects cytokinesis in both P2 and EMS.

PIE-1 does not affect relative surface tensions in P2

It was recently reported that in 4-cell stage embryos, cell surface tension is higher in the anterior ABa and ABp cells than in the posterior EMS and P2 cells (Yamamoto *et al.*, 2023). Because we found that these posterior cells were protected against cytokinesis failure in *formin(ts)* mutant embryos and that in P2 cytokinetic protection required key CCCH Zn-finger proteins, we hypothesized that this cytokinetic protection might be mediated by CCCH Zn-finger protein effects on P2 surface tension. We focused on PIE-1 for this analysis because MEX-1 and POS-1 are known to be required for proper PIE-1 localization (Guedes and Priess, 1997; Tenenhaus *et al.*, 1998; Tabara *et al.*, 1999; Oldenbroek *et al.*, 2012). To estimate the relative contribution of surface tension to different success rates of P2 cytokinesis, we measured the contact angles for both the P2-ABp and P2-EMS cell contacts in *formin(ts)* embryos with and without *pie-1(RNAi)* throughout the P2 cell cycle up until the onset of furrowing and used a Young–Dupré force balance to estimate surface tension ratios, similar to as was done previously (Chiou *et al.*, 2012; Kong *et al.*, 2019; Yamamoto *et al.*, 2023) (Figure 3A, see also *Materials and Methods*). We found no significant difference in the relative tensions of P2 surfaces between control and *pie-1(RNAi)* embryos (Figure 3, B–E). Cytokinesis failure was associated with altered tension patterns in the embryo (in ABp and/or P2 cells; Supplemental Figure S3A), but the precise tension patterns associated with successful cytokinesis seem to be distinct in control and *pie-1(RNAi)* embryos (Supplemental Figure S3, B and C). Together, our results do not suggest a major role for PIE-1 in regulating P2 surface tension.

PIE-1 does not affect overall spindle dynamics but has a minor effect on P2 cell size

Because signals from anaphase spindle microtubules are critical for cytokinesis in animal cells (Green *et al.*, 2012; D'Avino *et al.*, 2015),

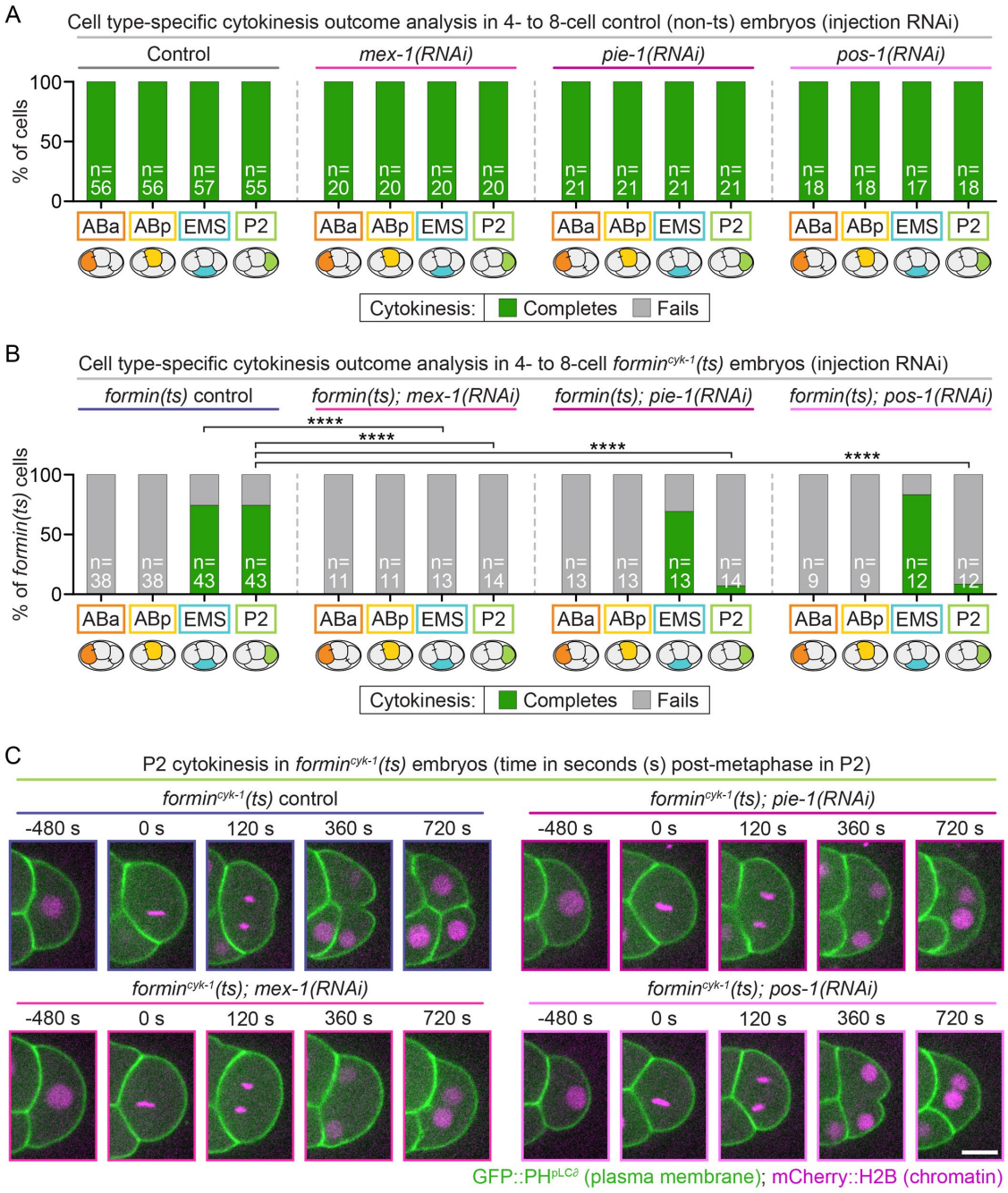

FIGURE 2: PIE-1 and POS-1 function cell type-specifically to protect cytokinesis in P2, whereas MEX-1 protects cytokinesis in both P2 and EMS. Graphs showing the percentage of ABa, ABp, EMS, and P2 cells that complete (green) or fail (gray) cytokinesis in 4- to 8-cell control embryos (A) and *formin*$^{cyk\text{-}1}$*(ts)* embryos (B) with and without *mex-1*, *pie-1*, or *pos-1* injection RNAi treatment; *n* = number of individual cells scored and is indicated on each bar; ****, *P*-value ≤0.0001 (Fisher's exact test; see also Supplemental Table S1). (C) Representative single plane images showing P2 cytokinesis in *formin*$^{cyk\text{-}1}$*(ts)* embryos with and without RNAi-mediated depletion of *mex-1*, *pie-1*, or *pos-1* in embryos expressing GFP::PH$^{PLC\delta}$ (green, plasma membrane) and mCherry::histone H2B$^{HIS\text{-}58}$ (magenta, chromatin); time (s) is relative to metaphase in each P2 cell; scale bar = 10 µm.

we tested whether PIE-1 mediates cytokinetic protection by regulating P2 spindle dynamics. During interphase, PIE-1 localizes to the nucleus and specialized ribonucleoprotein germ granules in the cytoplasm; during mitosis, PIE-1 localizes asymmetrically at P2 spindle poles and is enriched on the germ daughter P3-destined centrosome relative to the somatic daughter C-destined centrosome. (Mello *et al.*, 1996; Tenenhaus *et al.*, 1998) To test whether PIE-1 regulates the P2 anaphase spindle, we first examined overall spindle and cellular dynamics throughout P2 cell division (Figure 4A; Supplemental Figure S4A) with and without *pie-1(RNAi)* in a strain expressing fluorescently-tagged reporters to label the centrosomes (endogenously-tagged EB1$^{EBP\text{-}2}$::GFP [Sallee *et al.*, 2018]), chromatin (Audhya *et al.*, 2005), and plasma membrane (cell cortex) (Lee *et al.*, 2018). We found small differences in overall P2 spindle and cellular dynamics. Relative to dividing P2 cells in controls, P2 cells in *pie-1(RNAi)* embryos had a slight but significantly increased P2

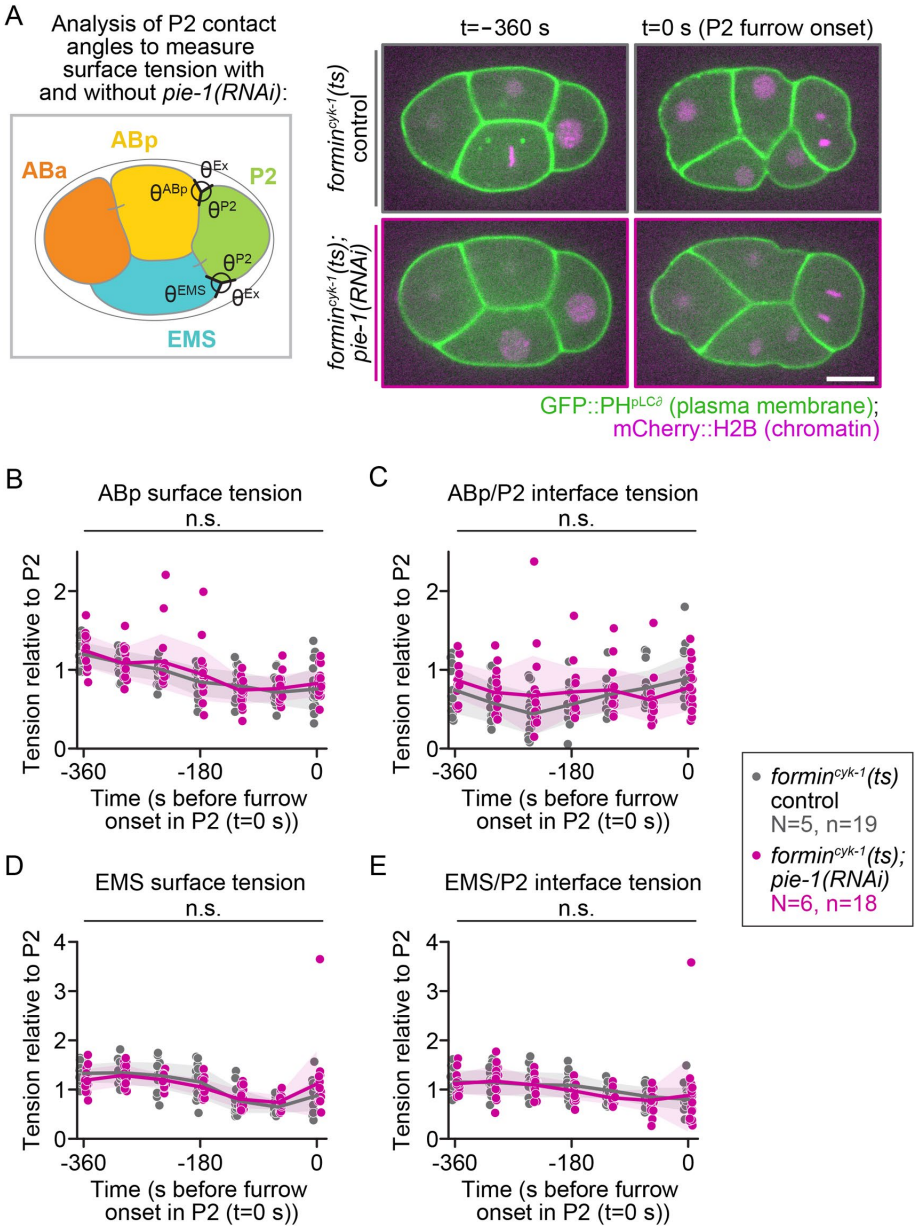

FIGURE 3: PIE-1 does not significantly change relative P2 cell surface tensions. (A) Schematic (left) and representative images (right) depicting how cell-cell contact angles with P2 (lime green) neighboring cells ABp (yellow) and EMS (teal) were measured (black angles) over time to calculate the relative cell surface and cell-cell interface tension in *formin*$^{cyk\text{-}1}$*(ts)* control (top panels, gray) and *formin*$^{cyk\text{-}1}$*(ts); pie-1(RNAi)* embryos (bottom panels, pink) expressing GFP::PH$^{PLC\delta}$ (green, plasma membrane) and mCherry::histone H2B$^{HIS\text{-}58}$ (magenta, chromatin) prior to P2 cytokinesis (similar to as was done in (Yamamoto *et al.*, 2023); tension measurements taken on *formin(ts)* control and *formin(ts); pie-1(RNAi)* datasets in Figure 2B and Figure 8; see also *Materials and Methods*); scale bar = 10 µm. Graphs showing the relative ABp surface tension (B), ABp/P2 interface tension (C), EMS surface tension (D), and EMS/P2 interface tension (E) in control (gray) and *pie-1(RNAi)* (pink) embryos. Tension measurements normalized to P2 surface tension; time (s) is relative to furrow onset (t = 0 s) in each P2 cell; *N* = number of experimental replicates; *n* = number of embryos scored for each genotype by color; n.s. = *P*-value not significant (Student's *t* test, unpaired with Holm-Sidak correction; see also Supplemental Table S1).

spindle length (centrosome to centrosome distance, Figure 4B), P2 cell length, P2 division plane diameter, and diameter of both forming C and P3 daughter cells (Supplemental Figure S4, B–E). The distance from the anterior cell cortex to the germ daughter P3-destined centrosome was also significantly increased in *pie-1(RNAi)* relative to control embryos, but there was no difference in the distance from the posterior cell cortex to the somatic daughter C-destined centrosome (Supplemental Figure S4, F and G). There were only minor differences in the separation of sister chromosomes in anaphase in *pie-1(RNAi)* relative to control embryos (Figure 4C). Importantly, spindle size is known to scale with cell size during early worm embryogenesis (Lacroix *et al.*, 2018). Thus, the small increase in spindle size after *pie-1(RNAi)* (7%) is likely due to the small increase in P2 cell size (9% increase in cell length and 10% increase in cell diameter at metaphase) rather than a direct effect of *pie-1(RNAi)* on overall spindle dynamics. We next tested whether PIE-1 regulates P2 astral microtubule dynamics by imaging the EB1$^{EBP\text{-}2}$::GFP microtubule plus-tip binding protein at higher temporal resolution. We found no difference in astral microtubule growth rates in P2 anaphase from either the C- or P3-destined centrosomal asters with and without *pie-1(RNAi)* (Figure 4D). Finally, we assessed central spindle assembly in control and *pie-1(RNAi)* embryos. The central spindle is an antiparallel microtubule structure that forms between separating chromatids in anaphase and also plays a role in contractile ring constriction (Green *et al.*, 2012; D'Avino *et al.*, 2015). Using a reporter for central spindle assembly (endogenously-tagged Aurora-B$^{AIR\text{-}2}$::GFP [Cheerambathur *et al.*, 2019]) (Maton *et al.*, 2015; Hirsch *et al.*, 2022), we found no difference in the timing or morphology of central spindle assembly in *pie-1(RNAi)* versus in control P2 cells (Figure 4, E and F; Supplemental Figure S5). Thus, PIE-1 has minor effects on P2 cell and spindle size, but despite localizing to the centrosomes, does not seem to have any major effects on overall P2 anaphase spindle dynamics.

PIE-1 plays a minor role in regulating daughter cell asymmetry during P2 cell division

Given the small differences in overall P2 and daughter cell size we observed during cell division with and without PIE-1, we tested whether PIE-1 affects P2 division asymmetry. The P2 cell divides asymmetrically, producing a larger somatic precursor daughter cell in the posterior and a smaller germ precursor daughter cell in the anterior (Arata *et al.*, 2010; Wang and Seydoux, 2013; Rose and Gonczy, 2014). PIE-1 is asymmetrically inherited by the germ precursor cells throughout early worm development (Mello *et al.*, 1996; Reese *et al.*, 2000; Wang and Seydoux, 2013; Gauvin *et al.*, 2018), but is not thought to regulate cell division asymmetry directly.

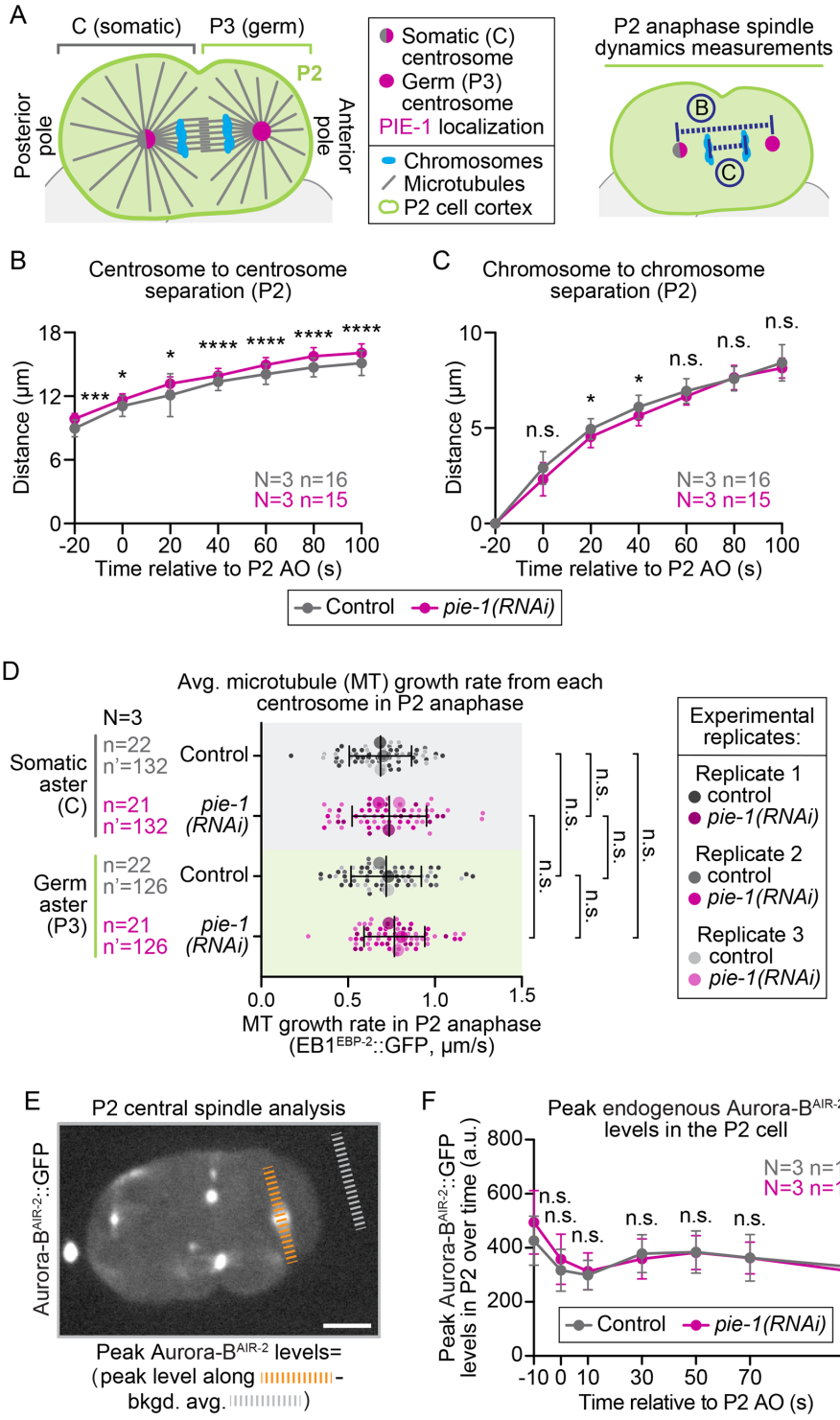

FIGURE 4: PIE-1 does not significantly alter P2 spindle or daughter cell dynamics. (A) Left, Schematic of a dividing P2 cell indicating the cell cortex (lime green), chromosomes (blue), centrosomes (C centrosome [half gray/half pink]; P3 centrosome [pink]), and microtubules (gray). Right, Schematic of measurements taken and plotted in B and C (see also *Materials and Methods*). Graphs plotting the kinetics of centrosome separation (B) and chromosome separation (C) over time (s) relative to anaphase onset (AO, t = 0 s) in dividing control (gray) and *pie-1(RNAi)* (pink) P2 cells expressing endogenously-tagged EB1^{EBP-2}::GFP, mCherry::histone H2B^{HIS-58}, and mCherry::PH$^{PLC\delta}$. Error bars = SD; *N* = number of experimental replicates; *n* = number of P2 cells scored for each genotype by color; n.s., not significant; *, *P*-value ≤ 0.05; ***, *P*-value ≤ 0.001; and ****, *P*-value ≤ 0.0001 (Student's *t* test, unpaired, see also Supplemental Table S1). (D) Graph showing super plots of the average growth rates for EB1^{EBP-2}::GFP-labeled astral microtubules emanating from the somatic- (C) or germ-daughter cell (P3) destined centrosome in dividing control (grays) and *pie-1(RNAi)* (pinks) P2 cells at 26°C. Small circles indicate individual data points and large circles and color shades indicate replicate averages; error bars = SD; *N* = number of experimental replicates; *n* = number of P2 cells scored; *n* = number of astral microtubules scored for each genotype by color; n.s. = not significant (two-way ANOVA, see also Supplemental Table S1). (E) Representative images (maximum projection) of a 4- to 8-cell embryo expressing endogenously-tagged Aurora-B^{AIR-2}::GFP and mCherry::H2B (not shown, see Supplemental Figure S5) depicting linescan analysis used on sum projected embryos to quantify central spindle (orange dashed line) and camera background (gray dashed line) shown in F; scale bar = 10 µm. (F) Graph plotting the average peak Aurora-B^{AIR-2}::GFP levels at chromosomes (preanaphase onset, AO [metaphase]) and the central spindle (post-AO) during P2 cell division in control (gray) and *pie-1(RNAi)* (pink) P2 cells over time. Time (s) is relative to anaphase onset (AO, t = 0 s) in each P2 cell; error bars = SD; *N* = number of experimental replicates; *n* = number of P2 cells scored for each genotype by color; n.s. = not significant (Student's *t* test, unpaired, see also Supplemental Table S1).

Myosin-II^{NMY-2} is a key regulator of asymmetric cell division in *C. elegans*. (Guo and Kemphues, 1996; Cuenca *et al.*, 2003; Munro *et al.*, 2004; Liu *et al.*, 2010; Rose and Gonczy, 2014) To test whether PIE-1 affects P2 cytokinesis by regulating polarity, we monitored polarity by measuring peak levels of myosin-II^{NMY-2}::GFP on the cortex in both forming daughter cells during P2 cytokinesis with and without *pie-1(RNAi)* (Figure 5, A and B). In control embryos, we found higher levels of myosin-II^{NMY-2} on the posterior C-destined daughter cell cortex than on the anterior P3-destined daughter cell cortex (Figure 5C), as would be predicted (Arata *et al.*, 2010; Liu *et al.*, 2010; Rose and Gonczy, 2014). In *pie-1(RNAi)* embryos, the levels of myosin-II^{NMY-2} were also higher on the C-destined daughter cell cortex than on the P3-destined daughter cell cortex, although to a lesser extent than in control embryos (Figure 5C). These results suggest that PIE-1 plays a minor role regulating myosin-II^{NMY-2} on the germ daughter-destined cell cortex but is not essential for overall cortical asymmetry during P2 cell division.

In the 1-cell embryo, we previously found that the cell polarity machinery was required to sequester anillin^{ANI-1} and septin^{UNC-59} on the anterior side of the cell cortex during cytokinesis (Jordan *et al.*, 2016). Thus, we also tested whether PIE-1 regulates the cortical

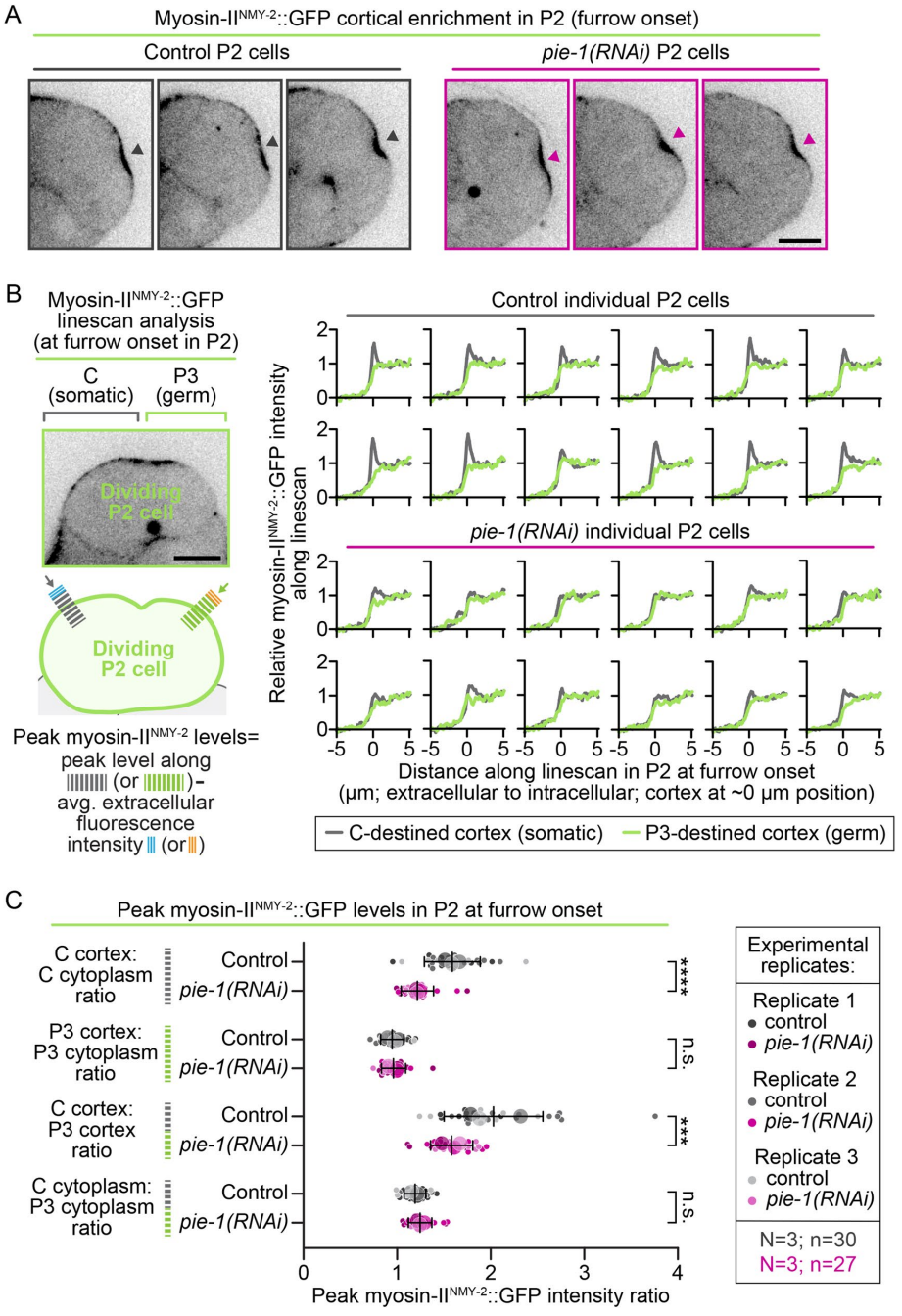

FIGURE 5: PIE-1 plays a minor role in P2 division asymmetry. (A) Representative single plane images of 3 control (left) and 3 *pie-1(RNAi)* (right) P2 cells expressing endogenously-tagged myosin-II^{NMY-2}::GFP at the time of cleavage furrow onset in P2; scale bar = 10 µm; gray (control) and pink (*pie-1(RNAi)*) arrowheads indicate the P2 cleavage furrow. (B) Left, Schematic depicting linescan analysis used to quantify cortical asymmetry of myosin-II^{NMY-2} in the P2 cell during division (image, top); arrows indicate direction of linescans drawn across the C-destined and P3-destined cell cortices from the respective extracellular to intracellular space (schematic, bottom; see also *Materials and Methods*). Right, Representative linescans from 12 control (top) and 12 *pie-1(RNAi)* (bottom) P2 cells plotting relative myosin-II^{NMY-2}::GFP levels along linescans across the C-destined (gray) and P3-destined (lime green) cell cortices. (C) Graph plotting peak cortical intensity ratios for myosin-II^{NMY-2}::GFP in control (gray) and *pie-1(RNAi)* (pink) embryos at the forming C and P3 daughter cell cortexes (relative to average cortical and cytoplasmic levels) during cell division. Error bars = SD; *N* = number of experimental replicates; *n* = number of embryos scored for each genotype by color; n.s., not significant; ***, *P*-value ≤0.001; and ****, *P*-value ≤0.0001 (Student's *t* test, unpaired, see also Supplemental Table S1).

asymmetry of anillin^{ANI-1} and/or septin^{UNC-59} in the P2 cell. In control embryos, we found higher levels of anillin^{ANI-1} on the posterior C-destined daughter cell cortex than on the anterior P3-destined daughter cell cortex (Supplemental Figure S6), similar to myosin-II^{NMY-2}. In *pie-1(RNAi)* embryos, similar to myosin-II^{NMY-2}, anillin^{ANI-1} levels were also higher on the C-destined daughter cell cortex than on the P3-destined daughter cell cortex, but to a lesser extent than in control embryos (Supplemental Figure S6). We found no detectable enrichment of septin^{UNC-59} on either the C or P3 sides of the dividing P2 cell cortex, with or without PIE-1 depletion (Supplemental Figure S6). This result suggests that cortical septin^{UNC-59} is not asymmetrically distributed during P2 division and, as with myosin-II^{NMY-2} and P2 cell size, PIE-1 may play a minor role in regulating asymmetric anillin^{ANI-1} levels on the somatic daughter-destined cell cortex.

PIE-1 and POS-1 reduce septin^{UNC-59} and anillin^{ANI-1} accumulation at the P2 cell division plane

While measuring the cortical asymmetry of contractile ring proteins during P2 cell division, we observed apparent changes in their protein levels at the P2 division plane following PIE-1 depletion. To test this, we quantified the effect of *pie-1(RNAi)* on contractile ring protein levels at the P2 cell division plane. We imaged the P2 contractile ring when the cleavage furrow was first visible by differential interference contrast (DIC) microscopy (furrow onset or 20 s postfurrow onset for septin^{UNC-59}::GFP) in strains expressing fluorescently-tagged reporters for multiple contractile ring proteins (LifeAct::RFP and plastin^{PLST-1}::GFP [F-actin] [Ding *et al.*, 2017], myosin-II^{NMY-2}::GFP [Dickinson *et al.*, 2013], septin^{UNC-59}::GFP [Chen *et al.*, 2019], and anillin^{ANI-1}::GFP [Rehain-Bell *et al.*, 2017]). Quantitative analysis revealed no significant difference in the levels of F-actin or the motor myosin-II^{NMY-2} at the P2 division plane in control versus in *pie-1(RNAi)* embryos (Figure 6, A–C and F). In contrast, RNAi knockdown of PIE-1 significantly increased the cortical levels of both endogenously-tagged septin^{UNC-59} and anillin^{ANI-1} at the P2 division plane relative to those of control embryos (~22% higher for septin^{UNC-59} and ~14% higher for anillin^{ANI-1} in *pie-1(RNAi)* embryos than in controls; Figure 6, D–F). Knockdown of PIE-1 also increased the total 4- to 8-cell whole embryo levels of septin^{UNC-59} (~16% higher), but not anillin^{ANI-1}, F-actin, or myosin-II^{NMY-2} (Supplemental Figure S7). Together, these results suggest that PIE-1, a critical regulator of

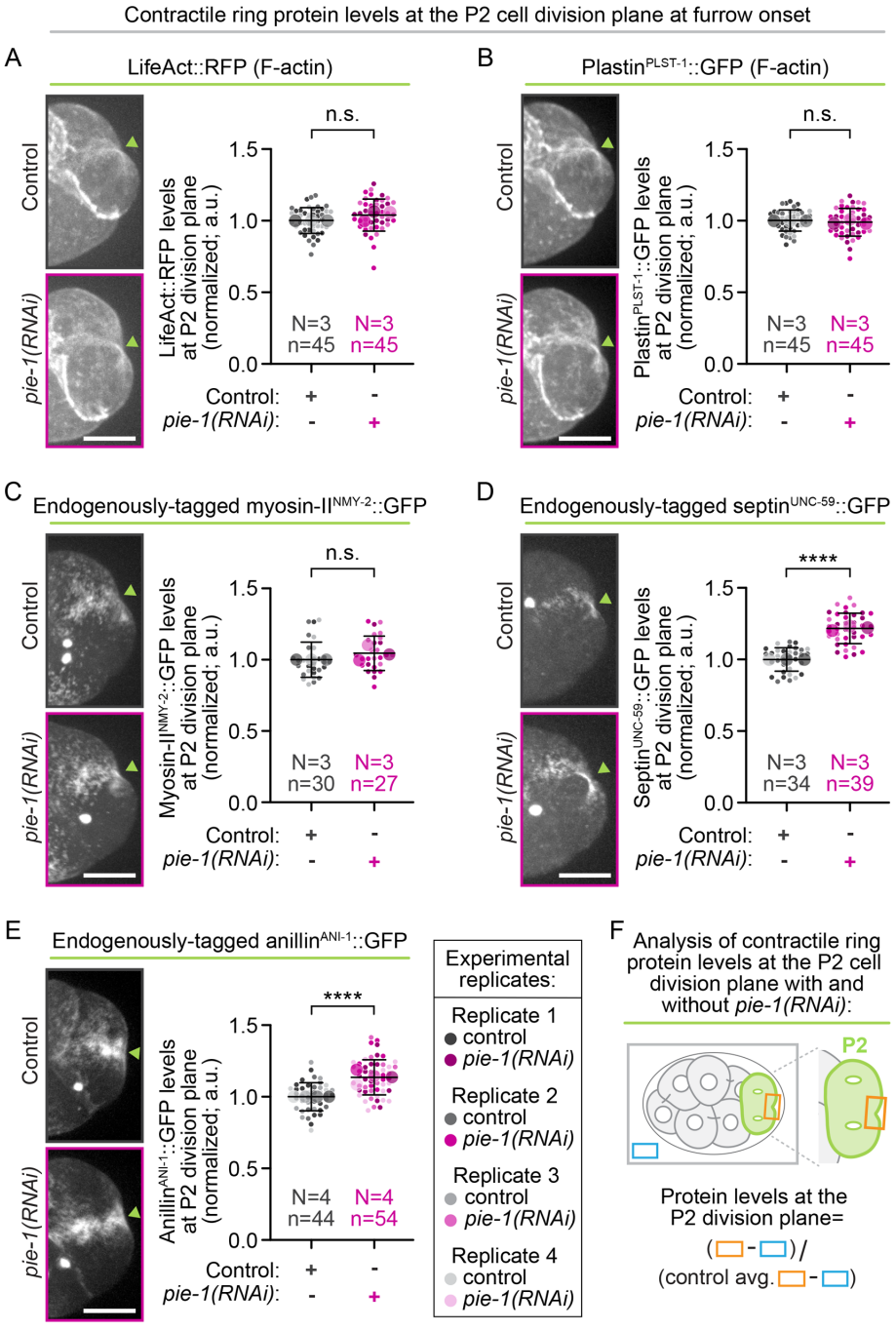

FIGURE 6: PIE-1 reduces the levels of septin^{UNC-59} and anillin^{ANI-1} in the P2 contractile ring. Representative maximum projection images (left) and graphs (right) showing super plots of normalized P2 contractile ring levels in control (grays) and *pie-1(RNAi)* (pinks) embryos expressing fluorescently-tagged reporters for A and B (F-actin Lifeact [A] and plastin^{PLST-1} [B]), myosin-II^{NMY-2} (C), septin^{UNC-59} (D), and anillin^{ANI-1} (E) at the time of cleavage furrow onset in P2 (or 20 s after furrow onset in P2 for endogenously-tagged septin^{UNC-59}). Lime green arrowheads on images indicate the P2 cleavage furrow; scale bar = 10 µm. In graphs, small circles indicate individual data points and large circles and color shades indicate replicate averages; error bars = SD; *N* = number of experimental replicates; *n* = number of embryos scored for each genotype by color; n.s., not significant; ****, *P*-value ≤ 0.0001 (Student's *t* test, unpaired, see also Supplemental Table S1). (F) Schematic depicting analysis shown in A–E performed on sum projected images to measure contractile ring protein levels in the P2 contractile ring (orange box) and extracellular background (blue box, see also *Materials and Methods*).

germ precursor cell fate, also functions to control the contractile ring levels of septin^{UNC-59} and its binding partner anillin^{ANI-1} during P2 cytokinesis.

While anillin often functions upstream of septins (Field *et al.*, 2005; Maddox *et al.*, 2005), anillin levels during cytokinesis are regulated by septin in some cellular contexts (e.g., see [Adam *et al.*, 2000; Piekny and Maddox, 2010; Kechad *et al.*, 2012]). To test whether PIE-1 and/or POS-1 act through septin^{UNC-59} to regulate the cortical levels of anillin^{ANI-1} at the P2 division plane in *formin(ts)* embryos, we imaged the levels of endogenously-tagged (Rehain-Bell *et al.*, 2017) anillin^{ANI-1} in *formin(ts)* embryos with and without RNAi knockdown of PIE-1, POS-1, and septin^{UNC-59} individually and together. RNAi knockdown was confirmed by loss of fluorescent signal in 4-cell embryos expressing fluorescently-tagged reporters of PIE-1 (Merritt *et al.*, 2008), POS-1 (Tsukamoto *et al.*, 2017), and septin^{UNC-59} (Chen *et al.*, 2019) (<1% of control levels in respective RNAi-mediated double knockdown embryos; Supplemental Figure S8). Anillin^{ANI-1} levels at the P2 division plane and in whole 4- to 8-cell embryos were much higher in *formin(ts)* mutants relative to those of control embryos with no ts mutations (Figure 7; Supplemental Figure S9), as was recently reported in formin^{CYK-1}-disrupted 1-cell embryos (Lebedev *et al.*, 2023). RNAi knockdown of septin^{UNC-59} reduced anillin^{ANI-1} levels at the P2 division plane, but not total embryo levels, in both control and *formin(ts)* embryos (~12% lower in control and ~21% lower in *formin(ts)* embryos; Figure 7; Supplemental Figure S9). RNAi knockdown of PIE-1 increased anillin^{ANI-1} levels at the P2 division plane to a similar extent in control (Figure 6E) and *formin(ts)* embryos (Figure 7) (~14% higher levels in control and ~13% in *formin(ts)* embryos). POS-1 knockdown also led to increased levels of anillin^{ANI-1} at the P2 division plane in *formin(ts)* embryos (~18% higher levels in *formin(ts); pos-1(RNAi)* embryos than in *formin(ts)* control embryos; Figure 7). The increase in anillin^{ANI-1} at the P2 division plane after PIE-1 or POS-1 knockdown was dependent on septin^{UNC-59}, as codepletion of either PIE-1 or POS-1 with septin^{UNC-59} in *formin(ts)* embryos reduced cortical anillin^{ANI-1} levels at the P2 division plane to a similar extent as depletion of septin^{UNC-59} on its own (~22% lower in *formin(ts); septin^{unc-59}(RNAi)*, ~19% lower in *formin(ts); pie-1(RNAi); septin^{unc-59}(RNAi)*, and ~20% lower in *formin(ts); pos-1(RNAi);*

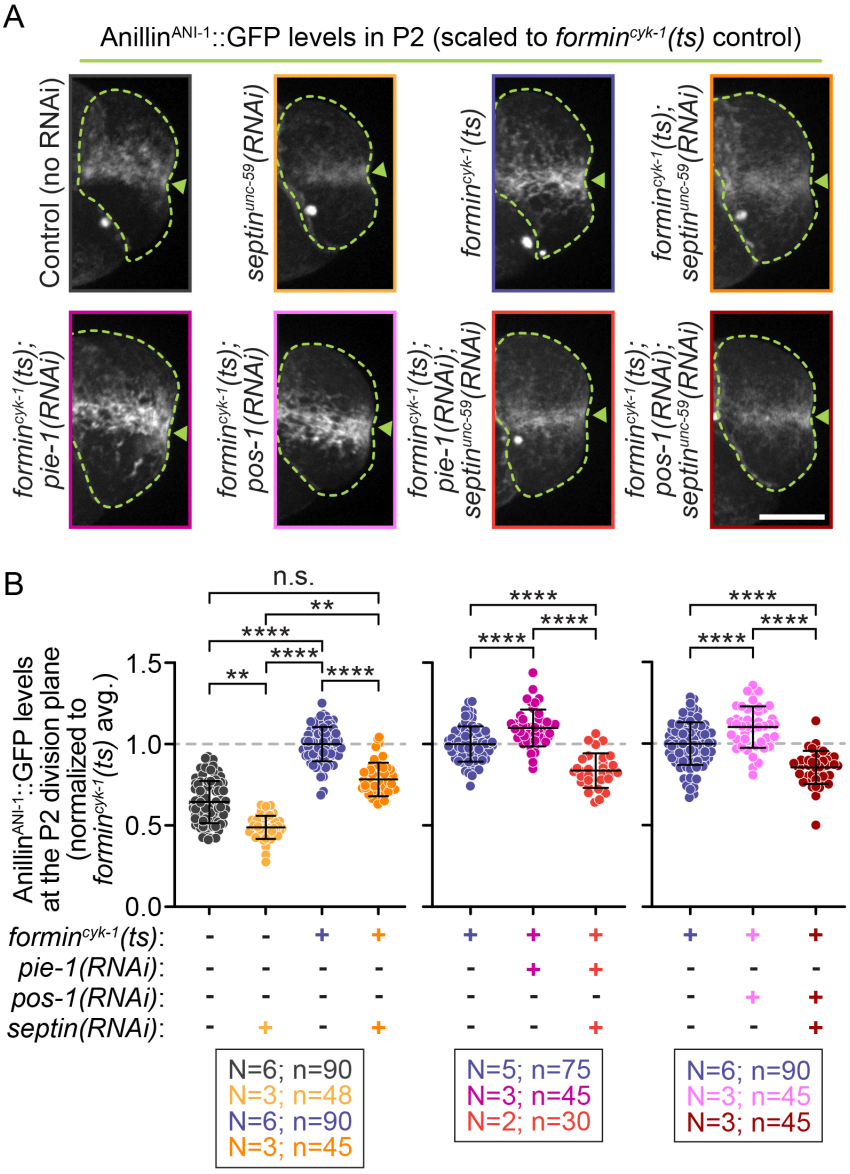

FIGURE 7: Septin^{UNC-59} is required for PIE-1 to reduce anillin^{ANI-1} levels in the P2 contractile ring. (A) Representative maximum projection images of endogenously-tagged anillin^{ANI-1}::GFP in P2 cells at cleavage furrow onset for indicated genotypes (images scaled relative to *formin^{cyk-1}(ts)* control embryos); scale bar = 10 µm; lime green arrowheads indicate the P2 cleavage furrow. (B) Graphs showing normalized anillin^{ANI-1}::GFP levels at the P2 division plane for each genotype (normalized to *formin^{cyk-1}(ts)* control embryos). Septin^{UNC-59} is required for the increased levels of anillin^{ANI-1} at the P2 division plane in *pie-1(RNAi); formin^{cyk-1}(ts)* and *pos-1(RNAi); formin^{cyk-1}(ts)* embryos. Error bars = SD; *N* = number of experimental replicates; *n* = number of embryos scored for each genotype by color; n.s., not significant; **, *P*-value ≤ 0.01; ****, *P*-value ≤0.0001 (two-way ANOVA, see also Supplemental Table S1).

septin^{unc-59}(RNAi) relative to in *formin(ts)* controls; Figure 7). Thus, PIE-1 and POS-1 require septin^{UNC-59} to control the levels of anillin^{ANI-1} in the P2 division plane in *formin(ts)* embryos.

Septin^{UNC-59} depletion is sufficient to rescue protection of P2 cytokinesis, even when codepleted with PIE-1 or POS-1

Given our results, we hypothesized that P2 cytokinetic protection in *formin(ts)* embryos is mediated by PIE-1 preventing excess septin^{UNC-59} (and therefore anillin^{ANI-1}) accumulation at the division plane. To directly test whether reducing septin^{UNC-59} levels could restore P2 cytokinetic protection in *formin(ts)* embryos after loss of PIE-1, we monitored P2 cytokinesis by time-lapse spinning disk confocal microscopy in embryos with and without single and double RNAi knockdown, as above (see also Supplemental Figure S8). In *formin(ts)* control embryos (with intact PIE-1 and POS-1), P2 was protected against cytokinesis failure and completed cytokinesis frequently (89% cytokinesis completion; Figure 8, A and B). P2 also completed cytokinesis frequently in *formin(ts)* embryos after RNAi knockdown of septin^{UNC-59} or anillin^{ANI-1} (92% and 90% cytokinesis completion, respectively; Figure 8, A and B). Again, this P2 cytokinetic protection in *formin(ts)* embryos was lost after knockdown of PIE-1 or POS-1 and cytokinesis failed at a significantly higher frequency (23% and 31% cytokinesis completion, respectively; Figure 8, A and B). In contrast, codepletion of septin^{UNC-59} with PIE-1 or POS-1 in *formin(ts)* embryos was sufficient to rescue the frequency of successful P2 division (92% and 93% cytokinesis completion, with PIE-1 or POS-1 depletion, respectively) (Figure 8, A and B), and allow P2 cytokinesis to occur in the absence of detectable F-actin at the division plane (Supplemental Figure S10, see also Discussion and Davies *et al.*, 2018). Together, our results support a model in which the PIE-1 and POS-1 germ fate determinants mediate P2 cytokinetic protection by reducing the levels of two cytoskeletal proteins that seem to act as negative regulators of contractile ring constriction at the division plane, septin^{UNC-59} and anillin^{ANI-1}. This germ fate-driven protection of the P2 germ precursor cell allows cytokinesis to complete successfully, even with greatly reduced F-actin levels at the cell division plane (Figure 8C).

DISCUSSION

Here, we investigated the mechanisms that drive cell type-specific protection of cytokinesis in the *C. elegans* P2 germ precursor cell. We identified three well-known germ fate determinants, MEX-1, PIE-1, and POS-1, as required for protection of P2 cytokinesis in *formin(ts)* embryos. Of these, PIE-1 and POS-1 specifically protected cytokinesis in P2, whereas MEX-1 also protected cytokinesis in EMS. Neither of these proteins has been previously implicated in cytokinesis and they are not required for cytokinesis in control embryos (e.g., see Figure 2A). We found that PIE-1 and POS-1 protect cytokinesis in P2 by preventing excessive accumulation of both septin^{UNC-59} and anillin^{ANI-1}, but not F-actin or myosin-II^{NMY-2}, at the cell division plane. Codepletion of septin^{UNC-59} and PIE-1 was both necessary and sufficient to reduce anillin^{ANI-1} levels at the P2 division plane and rescue the cytokinetic protection of P2. These data also demonstrate that septin^{UNC-59} and anillin^{ANI-1} can function as negative regulators of cytokinesis. Thus, we found these germ fate determinants protect cytokinesis by controlling the levels of specific actomyosin contractile ring-associated proteins to ensure cytokinesis completes successfully in this germ precursor cell, even without detectable F-actin in the contractile ring.

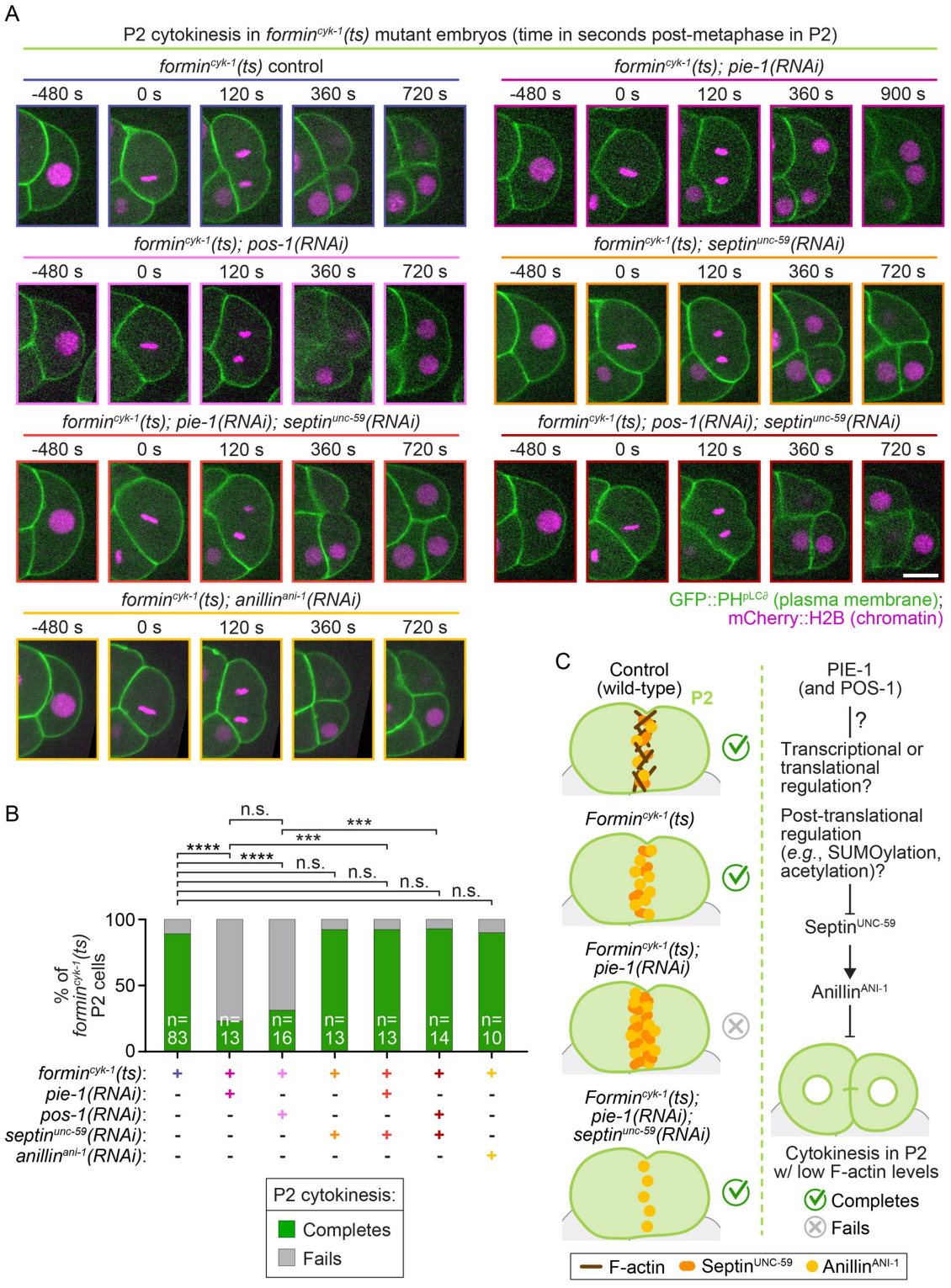

FIGURE 8: Reducing septin^{UNC-59} levels is sufficient to rescue protection of P2 cytokinesis. (A) Representative single plane images of cytokinesis after indicated RNAi treatment in *formin^{cyk-1}(ts)* P2 cells expressing GFP::PH$^{PLC\delta}$ (green, plasma membrane) and mCherry::histone H2B^{HIS-58} (magenta, chromatin). Time (s) is relative to metaphase in each P2 cell; scale bar = 10 µm. (B) Graphs plotting the percentage of P2 cells in *formin^{cyk-1}(ts)* embryos that complete (green) or fail (gray) in cytokinesis with or without indicated injection RNAi treatment. Codepletion of septin^{UNC-59} rescues robust P2 cytokinesis in *formin^{cyk-1}(ts); pie-1(RNAi)* and *formin^{cyk-1}(ts); pos-1(RNAi)* embryos. *n* = number of P2 cells scored and is indicated on each bar; n.s., not significant; ***, *P*-value ≤ 0.001; and ****, *P*-value ≤ 0.0001 (Fisher's exact test, see also Supplemental Table S1). (C) Schematic (left) and genetic (right) models for the function of PIE-1 and POS-1 in reducing septin^{UNC-59} and anillin^{ANI-1} levels at the P2 division plane to promote robust cytokinesis when contractile ring F-actin levels are greatly reduced (in *formin(ts)* embryos).

How do PIE-1 and POS-1 control the levels of septin^{UNC-59} and anillin^{ANI-1} in the P2 germ precursor cell? Canonically, both PIE-1 and POS-1 regulate germ cell fate by controlling transcription and translation (Batchelder *et al.*, 1999; Tabara *et al.*, 1999; Tenenhaus *et al.*, 2001; Unhavaithaya *et al.*, 2002; Ogura *et al.*, 2003; Zhang *et al.*, 2003; D'Agostino *et al.*, 2006; Farley *et al.*, 2008; Ghosh and Seydoux, 2008; Oldenbroek *et al.*, 2012; Elewa *et al.*, 2015). The early *C. elegans* germ precursor cells are thought to be transcriptionally silent and PIE-1 is required to maintain transcriptional repression in the germ precursor cells (Seydoux *et al.*, 1996; Tenenhaus *et al.*, 1998; Batchelder *et al.*, 1999; Ghosh and Seydoux, 2008; Guven-Ozkan *et al.*, 2008). POS-1 is required for PIE-1 to localize to the nucleus (Tenenhaus *et al.*, 2001), and thus also likely regulates its transcriptional control. Both POS-1 and PIE-1 are also implicated in translational regulation, and POS-1 is known to regulate poly-A tail length (Ogura *et al.*, 2003; D'Agostino *et al.*, 2006; Farley *et al.*, 2008). It is thus possible that germ fate normally leads to transcriptional or translational repression of a negative regulator of cytokinesis (e.g., *septin^{unc-59}* and/or *anillin^{ani-1}*). Consistent with this idea, the *septin^{unc-59}, septin^{unc-61}, and anillin^{ani-1}* genes all appear to have multiple cytoplasmic polyadenylation elements in their 3″-untranslated region (UTR) sequences, suggesting they might be regulated at the translational level. Indeed, in the absence of PIE-1, we observed higher protein levels of endogenously-tagged septin^{UNC-59}::GFP both at the P2 division plane and in the whole embryo level. Thus, transcriptional or translational regulation of cytokinesis genes could be controlled by these CCCH Zn-finger proteins.

PIE-1 also regulates posttranslational modifications in the germ line (e.g., acetylation, SUMOylation [Kim *et al.*, 2021]) by inhibiting the histone deacetylase HDA-1 and its associate NuRD complex as well as engaging with the SUMOylation machinery (Unhavaithaya *et al.*, 2002; Shin and Mello, 2003). PIE-1 itself is also SUMOylated and the SUMOylated lysine residue is required for full PIE-1 activity (Kim *et al.*, 2021). A recent proteomics study revealed that both anillin^{ANI-1} and septin^{UNC-59} are SUMOylated in the worm germline, and disruption of PIE-1 reduces the levels of SUMOylation on both anillin^{ANI-1} and septin^{UNC-59} (Kim *et al.*, 2021). Human anillin has also been found to be SUMOylated in a proteomics screen (Impens *et al.*, 2014), although the function of anillin SUMOylation is not clear. Septins are SUMOylated in other systems, including in budding yeast, where SUMOylation of several septin proteins (Cdc3, Cdc11, and Shs1) is cell cycle regulated (Johnson and Blobel, 1999). Mutation of the SUMOylated residues in these septins leads to synthetic cytokinetic failure at permissive temperature when combined with a ts mutant in a different yeast septin (*cdc-12*) that normally grows well at that temperature (Johnson and Blobel, 1999). Furthermore, septins from all four human septin groups are SUMOylated and expression of non-SUMOylatable septin (SEPT6 and SEPT7) variants leads to excessive septin bundling and an increase in multinucleated cells due to a late defect in cytokinesis (Ribet *et al.*, 2017). It will be interesting to test whether SUMOylation of PIE-1 and/or PIE-1-dependent SUMOylation of worm septins$^{UNC-59/-61}$ and/or anillin^{ANI-1} is responsible for protection of P2 cytokinesis.

How does the P2 cell divide without detectable F-actin in the division plane? A recent report suggested that, in the absence of formin^{CYK-1} activity, oligomerized anillin^{ANI-1} itself may interact with myosin-II^{NMY-2} motor proteins and drive cytokinesis in the 1-cell *C. elegans* embryo (Lebedev *et al.*, 2023). However, our finding that the P2 cell in *formin(ts)* mutants could still divide at a high frequency after RNAi knockdown of anillin^{ANI-1} (Figure 8, A and B) is inconsistent with that model. Moreover, in previous results, we found that inhibition of anillin^{ANI-1} could rescue cytokinesis failure in 1-cell embryos (grandmother cell of P2) after codisruption of cell polarity and formin^{CYK-1} activity (Jordan *et al.*, 2016), suggesting a similar mechanism may be at play. Recent in vitro evidence suggests that anillin is inhibitory to actomyosin contractility and that higher levels of myosin-II are required to induce contractility in the presence of anillin (Matsuda *et al.*, 2024). These data directly contradict a model in which anillin^{ANI-1} positively drives cytokinesis and are consistent with our proposed model in which septin^{UNC-59} and anillin^{ANI-1} function as negative regulators of cytokinesis, at least in *C. elegans* germ precursor cells.

The fundamental question remains, what is the positive driver of P2 cytokinesis in the absence of detectable F-actin, septin^{UNC-59}, and/or anillin^{ANI-1}? We cannot rule out that an adapted filamentous actin system forms upon formin^{CYK-1} disruption that does not associate with LifeAct, plastin^{PLST-1}, or utrophin-based (Burkel *et al.*, 2007) F-actin reporters (Supplemental Figure S10, see also Davies *et al.*, 2018). However, LifeAct binds to highly dynamic F-actin and the utrophin-based reporter binds to more stable actin filaments (Burkel *et al.*, 2007; Yoo *et al.*, 2010), so this would have to be a completely noncanonical type of actin filament. To us, it seems more likely that cytokinesis requires significantly lower levels of F-actin in certain cell type-specific contexts, such as in the P2 cell. Indeed, as myosin-II^{NMY-2} activity is required for cytokinesis in the P2 cell (Davies *et al.*, 2018), it seems highly likely that some F-actin remains in *formin(ts)* P2 cells that cannot be detected with existing weakly-fluorescent F-actin reporters. Further work will be needed to determine how and why cells like the P2 germ precursor cell can divide with reduced levels of F-actin in the contractile ring.

Cell type-specific protection of cytokinesis when the actin cytoskeleton is weakened in cells with a high potency, or ability to differentiate into other cell types, is not necessarily germ precursor cell-specific. Indeed, cell type-specific protection of cytokinesis with reduced F-actin levels may also apply to human embryonic stem cells. Inhibition of actomyosin contractility is routinely used in in vitro cell culture protocols to improve the survival of pluripotent embryonic stem cells, suggesting they can also divide with a weakened contractile ring (Chen *et al.*, 2010; Fan *et al.*, 2019). Thus, our findings in *C. elegans* germ precursor cells may provide insight into mechanisms of cytokinetic protection in other cell types, especially in stem cells that have a high potency, such as embryonic stem cells or induced pluripotent stem cells.

MATERIALS AND METHODS

Request a protocol through *Bio-protocol*.

Worm husbandry and strain maintenance

We note that Wormbase (wormbase.org [Davis *et al.*, 2022]) was used as a reference throughout this work. The *C. elegans* strains used in this study can be found in Supplemental Table S1. Strains were maintained on standard nonvented 60 mm plates (T3308, Tritech Research) filled (PourBoy 4, Tritech research) with 10.5 ml nematode growth media (NGM) (23 g Nematode Growth Medium [Legacy Biologicals, a division of Research Products International], 1 ml 1M $CaCl_2$, 1 ml of 1M $MgSO_4$ 25 ml of 1M K_3PO_4, 975 ml ddH_2O) seeded with 500 µl OP50 *Escherichia coli* bacteria as a food source, similar to as described (Brenner, 1974). Strains were maintained at 16°C (temperature sensitive mutants) or at 20°C (all other strains) in heating/cooling incubators (Binder).

RNAi

Feeding RNAi (mini-screen). For the mini-screen to identify genes required for protection of P2 cytokinesis in *formin(ts)* embryos

(Figure 1C), we used feeding RNAi to knockdown candidate genes either implicated in germ fate regulation in the literature or differentially expressed in the P2 cell (relative to the ABa cell) by single-cell transcriptomics (Tintori *et al.*, 2016). Briefly, ~1000 bp of sequence from the desired gene was amplified by PCR (from cDNA; E-RNAi was used to design primers [Horn and Boutros, 2010]), cloned into the L4440 vector using standard cloning techniques, and transformed into HT115 *E. coli* using $CaCl_2$ transformation, as described (Timmons *et al.*, 2001). RNAi feeding bacteria were grown in Luria Broth liquid cultures with 100 µg/ml ampicillin at 32°C for ~16 h and 300 µl of each culture was plated on an individual 60 mm RNAi plate (standard NGM plus 50 µg/ml ampicillin and 1 mM IPTG). HT115 *E. coli* with the empty L4440 vector was used as a feeding RNAi control. RNAi plates were allowed to dry and grow at room temperature for 48 h. *formin(ts)* L1 larvae were then plated onto RNAi plates and placed in the 16°C incubator for 6 d to become gravid adults before they were dissected to obtain embryos. RNAi primers and template DNA for each target gene are listed in Table S1.

Injection RNAi (all other experiments). For all other experiments in the manuscript, we used injection RNAi, which in our hands is more robust than feeding RNAi. Briefly, ~1000 bp of sequence from the desired was amplified by PCR (from cDNA and within a single exon when possible) using primers (E-RNAi was used to design primers [Horn and Boutros, 2010]) containing a T7 sequence, confirmed on a 1% agarose gel, PCR purified (QIAquick PCR Purification kit, QIAGEN), and used in T7 reverse transcription reactions (MEGAscript, Life Technologies). The synthesized double-stranded ribonucleic acids (dsRNAs) were purified using phenol-chloroform. The newly synthesized dsRNA was mixed 1:1 with phenol-chloroform (Invitrogen) and mixed by vortexing for 2 min. The dsRNA was spun down for 3 min at 12,000 × *g*. The aqueous layer was transferred to new tube, mixed again 1:1 with phenol-chloroform, and vortexed a second time for 2 min. The dsRNA was spun down for 3 min at 12,000 × *g* a second time. The aqueous layer was transferred to a new tube and then mixed 1:1 with prechilled (–20°C) isopropanol (100%, Sigma) and incubated at –20°C overnight. The dsRNA was precipitated by spinning the sample down at 12,000 × *g* for 15 min. The pellet was allowed to air dry for 5 min and then resuspended in 1x soaking buffer (32.7 mM Na_2HPO_4, 16.5 mM KH_2PO_4, 6.3 mM NaCl, 14.2 mM NH_4Cl). RNA reactions were annealed at 68°C for 10 min followed by 37°C for 30 min. dsRNAs were brought to a final concentration of ~2000–2500 ng/µl (when possible) and 2 µl aliquots of the dsRNA were stored at –80°C until use. For each experiment, a fresh aliquot (or aliquots for double RNAi experiments) was diluted to ~1000 ng/µl (~500 ng/µl for *pie-1* and *pos-1* dsRNA and ~1000 ng/µl for *septin*$^{unc-59}$ dsRNA in the double RNAi experiments) using 1x soaking buffer and centrifuged at 13,000 rpm for 10 min at room temp (~22°C). 0.35 µl of the diluted dsRNA was loaded into the back of pulled borosilicate glass capillary needles (World Precision Instruments, WPI; Sutter Instruments, P1000 needle puller) and injected into the gut of L4 worms using a Leica DMIRB microscope equipped with Hoffman optics, a Plan L 20x/0.4 CORR PH (Leica), a rotating stage, and the XenoWorks digital microinjector and micromanipulator injection system (Sutter Instruments). Worms were rescued by resuspension in M9 buffer (6 g KH_2PO_4, 12 g Na_2HPO_4, 10 g NaCl, 0.5 ml 1 M $MgSO_4$, ddH_2O to 2 L) to plates seeded with OP50 bacteria and allowed to recover for ~24 h at 20°C or ~42 h at 16°C (temperature sensitive strains) prior to imaging or embryonic lethality analysis. RNAi primers and template DNA for each target gene are listed in Supplemental Table S1.

Embryonic lethality analysis

Embryonic lethality quantifications for the mini-screen (feeding RNAi; Supplemental Figure S1B). On the morning of each experiment, 5 young adult/adult hermaphrodite worms from both the experimental group (*formin(ts)* plus candidate gene targeting-RNAi) and the control group (*formin(ts)* plus control RNAi [empty L4440 vector]) were singled out onto nonvented 35 mm NGM plates (T3501, Tritech Research) seeded with 100 µl of OP50 and placed back into the 16°C incubator (permissive temperature for the *formin(ts)* worms). Hermaphrodites were allowed to lay eggs for the duration of the day. In the evening (7–10 h later), the adult worm was removed from each plate. The following day, each plate was manually scored for hatched larvae and unhatched embryos on a high-resolution dissecting microscope (Olympus SZX16 with an Olympus SDF PLAPO 1XPF objective).

Embryonic lethality quantifications for injection RNAi. L4 hermaphrodite worms were injected with the indicated dsRNA and allowed to recover for 42 h at 16°C. 42-h postinjection, dsRNA-injected and control adult worms were then singled out and allowed to self-fertilize for 24 h, then the adult worms were disposed of. Prior to counting, embryos were given 36 h at 16°C to hatch. Plates were scored for hatched larvae and unhatched (dead) embryos on a high-resolution dissecting microscope, as above (feeding RNAi).

Embryo preparation for live-cell imaging

Young gravid adult hermaphrodites were kept at 13–14°C in a small incubator (Wine Enthusiast, model 2720213W) dissected on a high-resolution dissecting microscope (Olympus SZX16 with an Olympus SDF PLAPO 1XPF objective) in cooled (13–14°C) M9 buffer. 4-cell stage embryos were mounted on a thin (~1-2x lab tape thickness) 2% agar pad on a glass slide (VWR VistaVision, 3 inches × 1 inch × 1 mm) using a hand-pulled glass pipette (VWR Pasteur Pipette) or a borosilicate glass capillary (World Precision Instruments, WPI) as a mouth pipette. A 22 × 22 mm No. 1.5 glass coverslip (VWR) was placed on top of the embryos for imaging, similar to as described (Gonczy *et al.*, 1999).

Live-cell imaging set up and temperature control

We used two microscopes for live imaging experiments. Both microscope systems were controlled by MetaMorph software (Molecular Devices). Live imaging was performed in an imaging room equipped with a heat pump-based temperature control device (see below for details of each system). Room and microscope temperatures were continuously monitored using four to five digital thermometers placed around the room and near the microscope stage and a Bluetooth-enabled smart temperature sensor (SensorPush) on the microscope stage. All imaging was done at 26 ± 0.5°C, except for in Figure 2 and Figure 8 (and Figure 3; Supplemental Figure S3) which was done specifically at 25.5–26.0°C.

Live imaging microscopes

For the P2 cytokinesis RNAi mini-screen (Figure 1C), single-cell cytokinesis outcome experiments (Figure 2), central spindle assembly analysis (Figure 4, E and F; Supplemental Figure S5), half of the surface tension experiments (using the same *formin(ts)* control and *formin(ts); pie-1(RNAi)* data shown in Figure 2, B and C and presented in Figure 3; Supplemental Figure S3), and quantitative analysis of contractile ring protein levels (Figures 5, 6, and 7; Supplemental Figures S6, S7, S9, and S10), live-cell imaging was performed in an imaging room with a mini-split heat pump-based temperature control device (MultiAqua; model MHWX Hi-Wall Fan Coils).

The microscope was built on an inverted stand (Nikon, Eclipse Ti) with a spinning disk confocal (Yokogawa, CSU-10 with Borealis (Spectral Applied Research]), a charge-coupled device (CCD) camera (Hamamatsu Photonics, Orca-R2), and a Piezo-driven motorized stage (Applied Scientific Instrumentation, ASI) for Z-sectioning. Focus was maintained (Nikon, Perfect Focus) before each Z-series acquisition. Excitation laser light (150 mW 488 nm and 561 nm, Spectral Applied Research [ILE-2]) was controlled by an acousto-optic tunable filter (Spectral Applied Research), and a filter wheel (Sutter Instruments) was used for DIC analyzer and emission filter (525/50 nm and 620/60 nm bandpass [Chroma]) selection.

For quantitative analysis of protein levels after RNAi treatment (Supplemental Figures S2, A–D and S8), the other half of the surface tension experiments (using the same *formin(ts)* control and *formin(ts); pie-1(RNAi)* data shown in Figure 8, and presented in Figure 3; Supplemental Figure S3), spindle dynamics analysis (Figure 4, A–C; Supplemental Figure S4), microtubule growth rate analysis (Figure 4D), and some P2 cytokinesis outcome experiments (Figure 8), live-cell imaging was performed in an imaging room with a mini-split heat pump-based temperature control device (Mitsubishi; Mr. Slim, MSZ-D36NA). The microscope was built on an inverted stand (Nikon, Eclipse Ti; custom-modified for compatibility with near-infrared light, as in [Sundaramoorthy *et al.*, 2017; Hirsch *et al.*, 2018]) equipped with a spinning disk confocal unit (Yokogawa, CSU-10 with Borealis [Spectral Applied Research]), a CCD camera (Hamamatsu Photonics, Orca-R2), and a Piezo-driven motorized stage (ASI) for Z-sectioning. Focus was maintained (ASI, CRISP) before each Z-series acquisition. Two solid state 150 mW 488 nm and 561 nm lasers (Cairn) were used for excitation light, and a filter wheel (Ludl Instruments) was used for DIC polarizer and emission filter (525/50 nm and 620/50 nm bandpass [Chroma]) selection.

Live-cell imaging and analysis parameters

FIJI (FIJI is Just ImageJ) software (Schindelin *et al.*, 2012) was used for all data analyses.

Single-cell cytokinesis outcome analysis. For the P2 cell cytokinesis mini-screen (Figure 1C), we used a 20x Plan Apo 0.75 N.A. dry objective (Nikon) with 2 × 2 binning and 13 × 2 µm Z-sections every 60 s. For all other single-cell cytokinesis outcome analysis experiments and for half of the surface tension measurements (using the same datasets shown in Figure 8, shown in Figure 3; Supplemental Figure S3) we used a 60x Plan Apo 1.40 N.A. oil immersion objective (Nikon) with 2 × 2 binning and 15 × 2 µm Z-sections every 60 s. Cytokinesis outcome was scored manually by eye on maximum projection images of both channels (GFP::PH$^{PLC\delta}$ and mCherry::histone H2B^{HIS-58} [Audhya *et al.*, 2005]). Individual cells were only scored if the image series began before anaphase onset and ended after at least one of that cell's daughter cells entered anaphase of the next cell cycle, except for RNAi experiments in control embryos (Figure 2A), in which embryo viability was assumed. In those control embryos (Figure 2A), completion was scored if the image series began before anaphase onset and ended after a dividing membrane visible across all Z planes persisted between the cell's daughter cells for at least 180 s. In all other cytokinesis outcome analyses, cytokinesis in each individual cell was scored as either completed successfully (the cell under observation divided into two daughter cells and the contractile ring remained closed when a daughter cell entered anaphase of the next cell cycle) or failed (little to no contractile ring constriction or partial or full cleavage furrow ingression followed by contractile ring regression and binucleation).

Surface tension analysis. For P2 and neighboring cell surface tension analysis (Figure 3; Supplemental Figure S3) we used a 60x Plan Apo 1.40 N.A. oil immersion objective (Nikon) with 2 × 2 binning and 15 × 2 µm Z-sections every 60 s. The dataset used for this analysis came from two datasets used for analyses elsewhere in this paper: data collected for P2 cytokinesis outcome experiments shown in Figure 2, B and C and Figure 8. Image analysis was done on a single Z plane of the 4-cell embryo that was determined to be the most central to the longest and widest aspects of the P2 cell based on the fluorescently-tagged plasma membrane reporter. The timepoint at which the P2 cleavage furrow was first visible was considered t = 0 s (P2 furrow onset) and the previous 6 timepoints were also included in the analysis. At each timepoint, the FIJI (Schindelin *et al.*, 2012) angle tool was used to measure the three different membrane contact angles at each of the two locations that the P2 cell forms a cell-cell contact with a neighboring cell (either the ABp cell on the dorsal side or the EMS cell on the ventral side).

Cell surface tension analysis was done similarly to as recently described (Yamamoto *et al.*, 2023) with a few modifications. Measured angles were rescaled to add to 360° for self-consistency. A Young-Dupré force balance was used to relate P2 surface tension to EMS/ABp surface and interfacial tensions using the measured contact angles:

$$\gamma_{P2} + \gamma_{ABp}cos\theta_{Ex} + \gamma_{ABp/p2}cos\theta_{p2} = 0 \quad (1)$$

$$\gamma_{ABp}\sin\theta_{Ex} - \gamma_{ABp/p2}sin\theta_{p2} = 0 \quad (2)$$

$$\gamma_{P2} + \gamma_{EMS}cos\theta_{Ex} + \gamma_{EMS/p2}cos\theta_{p2} = 0 \quad (3)$$

$$\gamma_{EMS}sin\theta_{Ex} - \gamma_{EMS/p2}sin\theta_{p2} = 0 \quad (4)$$

Quantitative analysis of fluorescently-tagged reporters for RNAi knockdown efficiency. For quantitative imaging of fluorescently-tagged MEX-1 (Wu *et al.*, 2015), PIE-1 (Merritt *et al.*, 2008), POS-1 (Tsukamoto *et al.*, 2017), and septin^{UNC-59} (Chen *et al.*, 2019) reporters with and without the respective single-stranded or dsRNA injection (Supplemental Figures S2, A–D and S8), we used a 60x Plan Apo 1.40 N.A. oil immersion objective (Nikon) with 2 × 2 binning and 15 × 2 µm Z-sections. Image analysis was done on sum projection images of 4-cell stage embryos from each individual fluorescently-tagged CCCH Zn-finger protein or endogenously-tagged septin^{UNC-59} reporter strain with and without RNAi-mediated depletion of that Zn-finger protein or septin^{UNC-59}. A region surrounding the P2 cell (for CCCH Zn-finger proteins) or whole embryo (for *septin^{unc-59}* knockdown) was manually drawn to measure the total fluorescence intensity and a 20 × 20-pixel box was drawn in the cytoplasm of the ABa cell to calculate intracellular embryonic background levels. The average ABa cytoplasmic fluorescence background intensity was multiplied by the measured area of the P2 cell (for CCCH Zn-finger proteins) or whole embryo (for *septin^{unc-59}* knockdown) area and then subtracted from each P2 cell (or whole embryo) fluorescence intensity measurement.

P2 spindle and cellular dynamics imaging and analysis. For analysis of P2 spindle and cellular dynamics with and without *pie-1(RNAi)* (Figure 4, A–C; Supplemental Figure S4), we used a 60x Plan Apo 1.40 N.A. oil immersion objective (Nikon) with 1 × 1 binning and 13 × 1.5 µm Z-sections every 20 s. This analysis was done in a strain

expressing mCherry::histone H2B (Audhya *et al.*, 2005) to label the chromosomes, mCherry::PH$^{PLC\delta}$ (Lee *et al.*, 2018) to label the plasma membrane, and endogenously-tagged EB1^{EBP-2}::GFP (Sallee *et al.*, 2018) to label the centrosomes. All measurements were taken using the line drawing tool in FIJI (Schindelin *et al.*, 2012). Composite images were made of both mCherry and GFP channels at all Z planes and measurements were taken on the Z plane where both objects of interest (chromosomes, centrosomes, or plasma membrane) were best visible and in focus (e.g., the Z plane containing the P3-destined centrosome and chromosomes or the C-destined centrosome and chromosomes). Forming daughter cell size measurements were taken on the Z plane in which the distance between the plasma membrane was the greatest (widest part of the cell). For the centrosome to centrosome, chromatin to chromatin, and P2 cell long axis measurements specifically, maximum intensity projections were used to enable visualization of objects in different Z planes.

Microtubule growth rate imaging and analysis. For analysis of astral microtubule growth rates with and without *pie-1(RNAi)* (Figure 4D), we used a 60x Plan Apo 1.40 N.A. oil immersion objective (Nikon) with 1 × 1 binning and a single Z-plane every 0.5 s for at least 2 min. Embryos were monitored by DIC and mCherry::histone H2B^{HIS-58} (Audhya *et al.*, 2005) until anaphase onset, at which point time-lapse imaging was initiated. Image analysis was done using the "Manual Tracking" plugin in FIJI (Schindelin *et al.*, 2012). The plugin was used to measure velocities of microtubule plus tips that could be clearly seen for three frames, based on the distance traveled per frame, the temporal resolution between frames, and the XY calibration of the microscope. Two velocities for each microtubule plus tip were calculated by clicking on the center of the microtubule plus tip across three frames; the plugin calculated one velocity between the first and second frames and a second velocity between the second and third frames. An average velocity for each microtubule plus tip was then determined by averaging the two velocities calculated with the plugin.

Central spindle assembly imaging and analysis. For analysis of central spindle assembly with and without *pie-1(RNAi)* (Figure 4, E and F; Supplemental Figure S5), we used a 40x Plan Fluor 1.30 N.A. oil immersion objective (Nikon) with 2 × 2 binning and 10 × 1.25 µm Z-sections every 10 s. Embryos were monitored by DIC and mCherry::histone H2B (Hirsch *et al.*, 2022) until the initiation of nuclear envelope breakdown, at which point endogenously-tagged Aurora-B^{AIR-2}::GFP (Cheerambathur *et al.*, 2019) imaging was started. Quantitative measurements of peak Aurora-B^{AIR-2}::GFP and mCherry::histone H2B levels began at the frame prior to anaphase onset (metaphase). For each measurement and timepoint, a linescan of 10 µm wide and 80 µm long was drawn from the "EMS side" to the "ABp side" of the P2 cell, perpendicular to the division plane in both the GFP and mCherry channels. An extracellular background linescan was also taken for each channel. The background linescan for each channel was averaged and then subtracted from each pixel value along the P2 central spindle linescan in each channel.

Quantitative analysis of fluorescently-tagged contractile ring protein levels. For quantitative imaging of fluorescently-tagged F-actin reporters (LifeAct::RFP and plastin^{PLST-1}::GFP [Ding *et al.*, 2017]), myosin-II^{NMY-2}::GFP (endogenously-tagged [Dickinson *et al.*, 2013]), septin^{UNC-59}::GFP (endogenously-tagged [Chen *et al.*, 2019]), and anillin^{ANI-1}::GFP (endogenously-tagged [Rehain-Bell *et al.*, 2017]) with and without dsRNA injection in control and *formin(ts)* embryos (Figures 5–7; Supplemental Figures S6, S7, S9, and S10), we used a 60x Plan Apo 1.40 N.A. oil immersion objective (Nikon) with 2 × 2 binning and a single 45 × 0.5 µm Z-section timepoint was taken. Embryos were monitored by DIC and images were acquired at the time of cleavage furrow onset in the P2 cell (LifeAct::RFP, plastin^{PLST-1}::GFP, myosin-II^{NMY-2}::GFP, and anillin^{ANI-1}::GFP) or 20 s after P2 furrow onset (septin^{UNC-59}::GFP). For image analysis, first embryos were rotated so the P2 division plane was located on the right side of the image. Next sum projections were created for each embryo. A 25 × 50-pixel box was drawn over the P2 cleavage furrow/division plane and the total fluorescence intensity was measured. To measure the total fluorescence intensity of the entire embryo, an oval was drawn around the embryo. A 25 × 50-pixel box was then placed outside of the embryo to measure the extracellular background (camera background) and value was then subtracted from the total fluorescence intensity in the division plane. For the whole embryo total fluorescence intensity, background was subtracted by multiplying the mean intensity of the extracellular background by the area of the embryo. Each individual value was than normalized to the control average for its respective experimental replicate. For Figure 7, individual data points are shown and normalized to the *formin(ts)* average.

To measure the asymmetric localization of endogenously-tagged myosin-II^{NMY-2}::GFP, septin^{UNC-59}::GFP, and anillin^{ANI-1}::GFP on the dividing P2 cell cortex, two independent 25-pixel wide × 10 µm long lines were drawn across the future C-cell cortex and the future P3-cell cortex from outside of the cell into cytoplasm (see schematic in Figure 5B). The first 10 pixels of each linescan from outside of the cell were averaged to calculate the average extracellular background (camera background). The average extracellular background was then subtracted from all other points along the same line. The last 15 pixels of the line (~2.4 µm; inside the cell) were averaged to calculate the "average cytoplasmic value" for each forming daughter cell. The maximum value at the cell cortex was used as the "peak cortical level." The peak cortical level measurement was divided by the average cytoplasmic level to calculate the cell cortex to cytoplasmic ratio for each forming daughter cell. The peak cortical value for the forming C cell was divided by the peak cortical value for the forming P3 cell to calculate the ratio between the two. The C-destined cytoplasmic value was divided by the P3-destined cytoplasmic value to calculate the ratio between the two. To plot the linescan data on one graph, each point along the line was normalized using the respective cytoplasmic value.

Figure preparation

All figures were made using Adobe Illustrator 2023; graphs were made in Prism 9 (Graphpad) or in Python using Matplotlib (Hunter, 2007) (tension analysis only) and pasted into Adobe Illustrator.

Statistical analysis

All statistical tests were done in Prism 9 (Graphpad) or by using Excel (Microsoft). For all single-cell cytokinesis outcome experiments, a Fisher's exact test was used. For analysis of significance in most experiments an unpaired Student's *t* test was used (with a Holm-Sidak correction for surface tension analysis only) except for the quantitative analysis of mean microtubule growth rates and anillin^{ANI-1} levels at the P2 division plane where a two-way ANOVA was used. Error bars in all graphs represent the SD (SD). *P* values: n.s., $P > 0.05$; *, $P \leq 0.05$; **, $P \leq 0.01$; ***, $P \leq 0.001$; and ****, $P \leq 0.0001$; except for tension analysis (n.s., *P*-value not significant; *, *P*-value significant; Figure 3; Supplemental Figure S3); see also Supplemental Table S1.

ACKNOWLEDGMENTS

We thank all members of the Canman and Shirasu-Hiza labs for their feedback, support, and advice on this work. We thank Adriana Hernandez and Michelle (Mimi) Schmidt for making worm plates and other critical lab reagents. We thank Mohan Balasubramanian and Geraldine Seydoux for helpful discussions. We are grateful to Jessica Feldman, Geraldine Seydoux, Amy Maddox, Karen Oegema, and the Caenorhabditis Genetics Center (NIH P40OD010440) for providing worm strains. This work was funded by: NIH R01GM117407 (J.C.C.), NSF DGE-2036197 (J.T.W.), NIH R35GM138380 (K.E.K.), a Sloan Research Fellowship (K.E.K.), a Packard Fellowship (K.E.K.), European Research Council CoG ChromoSOMe N°819179 (J.D.), NIH R01AG045842 (M.S.H.), and NIH R35GM127049 (M.S.H.).

REFERENCES

Ackman JB, Ramos RL, Sarkisian MR, Loturco JJ (2007). Citron kinase is required for postnatal neurogenesis in the hippocampus. Dev Neurosci 29, 113–123.

Adam JC, Pringle JR, Peifer M (2000). Evidence for functional differentiation among Drosophila septins in cytokinesis and cellularization. Mol Biol Cell 11, 3123–3135.

Andrade V, Echard A (2022). Mechanics and regulation of cytokinetic abscission. Front Cell Dev Biol 10, 1046617.

Arata Y, Lee JY, Goldstein B, Sawa H (2010). Extracellular control of PAR protein localization during asymmetric cell division in the C. elegans embryo. Development 137, 3337–3345.

Audhya A, Hyndman F, McLeod IX, Maddox AS, Yates JR, 3rd, Desai A, Oegema K (2005). A complex containing the Sm protein CAR-1 and the RNA helicase CGH-1 is required for embryonic cytokinesis in Caenorhabditis elegans. J Cell Biol 171, 267–279.

Basit S, Al-Harbi KM, Alhijji SA, Albalawi AM, Alharby E, Eldardear A, Samman MI (2016). CIT, a gene involved in neurogenic cytokinesis, is mutated in human primary microcephaly. Hum Genet 135, 1199–1207.

Batchelder C, Dunn MA, Choy B, Suh Y, Cassie C, Shim EY, Shin TH, Mello C, Seydoux G, Blackwell TK (1999). Transcriptional repression by the Caenorhabditis elegans germ-line protein PIE-1. Genes Dev 13, 202–212.

Bauer J, Lacroix L, Labbe JC (2021). The primordial germ line is refractory to perturbations of actomyosin regulator function in C. elegans L1 larvae. MicroPubl Biol 2021.

Bione S, Sala C, Manzini C, Arrigo G, Zuffardi O, Banfi S, Borsani G, Jonveaux P, Philippe C, Zuccotti M, *et al.* (1998). A human homologue of the Drosophila melanogaster diaphanous gene is disrupted in a patient with premature ovarian failure: evidence for conserved function in oogenesis and implications for human sterility. Am J Hum Genet 62, 533–541.

Bowerman B (1995). Determinants of blastomere identity in the early C. elegans embryo. Bioessays 17, 405–414.

Brenner S (1974). The genetics of Caenorhabditis elegans. Genetics 77, 71–94.

Burkel BM, von Dassow G, Bement WM (2007). Versatile fluorescent probes for actin filaments based on the actin-binding domain of utrophin. Cell Motil Cytoskeleton 64, 822–832.

Cheerambathur DK, Prevo B, Chow TL, Hattersley N, Wang S, Zhao Z, Kim T, Gerson-Gurwitz A, Oegema K, Green R, Desai A (2019). The kinetochore-microtubule coupling machinery is repurposed in sensory nervous system morphogenesis. Dev Cell 48, 864–872.e7.

Chen D, Hastie E, Sherwood D (2019). Endogenous expression of UNC-59/Septin in C. elegans. MicroPubl Biol 2019.

Chen G, Hou Z, Gulbranson DR, Thomson JA (2010). Actin-myosin contractility is responsible for the reduced viability of dissociated human embryonic stem cells. Cell Stem Cell 7, 240–248.

Chiou KK, Hufnagel L, Shraiman BI (2012). Mechanical stress inference for two dimensional cell arrays. PLoS Comput Biol 8, e1002512.

Cuenca AA, Schetter A, Aceto D, Kemphues K, Seydoux G (2003). Polarization of the C. elegans zygote proceeds via distinct establishment and maintenance phases. Development 130, 1255–1265.

D'Agostino I, Merritt C, Chen PL, Seydoux G, Subramaniam K (2006). Translational repression restricts expression of the C. elegans Nanos homolog NOS-2 to the embryonic germline. Dev Biol 292, 244–252.

D'Avino PP, Giansanti MG, Petronczki M (2015). Cytokinesis in animal cells. Cold Spring Harb Perspect Biol 7, a015834.

Davies T, Jordan SN, Chand V, Sees JA, Laband K, Carvalho AX, Shirasu-Hiza M, Kovar DR, Dumont J, Canman JC (2014). High-resolution temporal analysis reveals a functional timeline for the molecular regulation of cytokinesis. Dev Cell 30, 209–223.

Davies T, Kim HX, Romano Spica N, Lesea-Pringle BJ, Dumont J, Shirasu-Hiza M, Canman JC (2018). Cell-intrinsic and -extrinsic mechanisms promote cell-type-specific cytokinetic diversity. Elife 7, e36204.

Davis P, Zarowiecki M, Arnaboldi V, Becerra A, Cain S, Chan J, Chen WJ, Cho J, da Veiga Beltrame E, Diamantakis S, *et al.* (2022). WormBase in 2022-data, processes, and tools for analyzing Caenorhabditis elegans. Genetics 220, iyac003.

DeRenzo C, Reese KJ, Seydoux G (2003). Exclusion of germ plasm proteins from somatic lineages by cullin-dependent degradation. Nature 424, 685–689.

Di Cunto F, Imarisio S, Hirsch E, Broccoli V, Bulfone A, Migheli A, Atzori C, Turco E, Triolo R, Dotto GP, *et al.* (2000). Defective neurogenesis in citron kinase knockout mice by altered cytokinesis and massive apoptosis. Neuron 28, 115–127.

Dickinson DJ, Ward JD, Reiner DJ, Goldstein B (2013). Engineering the Caenorhabditis elegans genome using Cas9-triggered homologous recombination. Nat Methods 10, 1028–1034.

Dieterich K, Zouari R, Harbuz R, Vialard F, Martinez D, Bellayou H, Prisant N, Zoghmar A, Guichaoua MR, Koscinski I, *et al.* (2009). The Aurora Kinase C c.144delC mutation causes meiosis I arrest in men and is frequent in the North African population. Hum Mol Genet 18, 1301–1309.

Ding WY, Ong HT, Hara Y, Wongsantichon J, Toyama Y, Robinson RC, Nedelec F, Zaidel-Bar R (2017). Plastin increases cortical connectivity to facilitate robust polarization and timely cytokinesis. J Cell Biol 216, 1371–1386.

Elewa A, Shirayama M, Kaymak E, Harrison PF, Powell DR, Du Z, Chute CD, Woolf H, Yi D, Ishidate T, *et al.* (2015). POS-1 promotes endo-mesoderm development by inhibiting the cytoplasmic polyadenylation of neg-1 mRNA. Dev Cell 34, 108–118.

Fan YL, Zhao HC, Li B, Zhao ZL, Feng XQ (2019). Mechanical roles of F-actin in the differentiation of stem cells: a review. ACS Biomater Sci Eng 5, 3788–3801.

Fares H, Goetsch L, Pringle JR (1996). Identification of a developmentally regulated septin and involvement of the septins in spore formation in Saccharomyces cerevisiae. J Cell Biol 132, 399–411.

Farley BM, Pagano JM, Ryder SP (2008). RNA target specificity of the embryonic cell fate determinant POS-1. RNA 14, 2685–2697.

Ferrer I, Mohan P, Chen H, Castellsague J, Gomez-Baldo L, Carmona M, Garcia N, Aguilar H, Jiang J, Skowron M, *et al.* (2014). Tubers from patients with tuberous sclerosis complex are characterized by changes in microtubule biology through ROCK2 signalling. J Pathol 233, 247–257.

Field CM, Coughlin M, Doberstein S, Marty T, Sullivan W (2005). Characterization of anillin mutants reveals essential roles in septin localization and plasma membrane integrity. Development 132, 2849–2860.

Foe VE (1989). Mitotic domains reveal early commitment of cells in Drosophila embryos. Development 107, 1–22.

Ganem NJ, Cornils H, Chiu SY, O'Rourke KP, Arnaud J, Yimlamai D, Thery M, Camargo FD, Pellman D (2014). Cytokinesis failure triggers hippo tumor suppressor pathway activation. Cell 158, 833–848.

Ganem NJ, Storchova Z, Pellman D (2007). Tetraploidy, aneuploidy and cancer. Curr Opin Genet Dev 17, 157–162.

Gauvin TJ, Han B, Sun MJ, Griffin EE (2018). PIE-1 translation in the germline lineage contributes to PIE-1 asymmetry in the early caenorhabditis elegans embryo. G3 8, 3791–3801.

Gerhold AR, Labbe JC, Singh R (2022). Uncoupling cell division and cytokinesis during germline development in metazoans. Front Cell Dev Biol 10, 1001689.

Ghosh D, Seydoux G (2008). Inhibition of transcription by the Caenorhabditis elegans germline protein PIE-1: genetic evidence for distinct mechanisms targeting initiation and elongation. Genetics 178, 235–243.

Giansanti MG, Bonaccorsi S, Gatti M (1999). The role of anillin in meiotic cytokinesis of Drosophila males. J Cell Sci 112, 2323–2334.

Gonczy P, Schnabel H, Kaletta T, Amores AD, Hyman T, Schnabel R (1999). Dissection of cell division processes in the one cell stage Caenorhabditis elegans embryo by mutational analysis. J Cell Biol 144, 927–946.

Green RA, Paluch E, Oegema K (2012). Cytokinesis in animal cells. Annu Rev Cell Dev Biol 28, 29–58.

Gu Y, Yam C, Oliferenko S (2015). Rewiring of cellular division site selection in evolution of fission yeasts. Curr Biol 25, 1187–1194.

Guedes S, Priess JR (1997). The C. elegans MEX-1 protein is present in germline blastomeres and is a P granule component. Development 124, 731–739.

Guo S, Kemphues KJ (1996). A non-muscle myosin required for embryonic polarity in Caenorhabditis elegans. Nature 382, 455–458.
Guven-Ozkan T, Nishi Y, Robertson SM, Lin R (2008). Global transcriptional repression in C. elegans germline precursors by regulated sequestration of TAF-4. Cell 135, 149–160.
Hachet O, Simanis V (2008). Mid1p/anillin and the septation initiation network orchestrate contractile ring assembly for cytokinesis. Genes Dev 22, 3205–3216.
Harding BN, Moccia A, Drunat S, Soukarieh O, Tubeuf H, Chitty LS, Verloes A, Gressens P, El Ghouzzi V, Joriot S, *et al*. (2016). Mutations in citron kinase cause recessive microlissencephaly with multinucleated neurons. Am J Hum Genet 99, 511–520.
Hirsch SM, Edwards F, Shirasu-Hiza M, Dumont J, Canman JC (2022). Functional midbody assembly in the absence of a central spindle. J Cell Biol 221, e202011085.
Hirsch SM, Sundaramoorthy S, Davies T, Zhuravlev Y, Waters JC, Shirasu-Hiza M, Dumont J, Canman JC (2018). FLIRT: fast local infrared thermogenetics for subcellular control of protein function. Nat Methods 15, 921–923.
Horn T, Boutros M (2010). E-RNAi: a web application for the multi-species design of RNAi reagents–2010 update. Nucleic Acids Res 38, W332–W339.
Hunter JD (2007). Matplotlib: a 2D graphics environment. Comput Sci Eng 9, 90–95.
Impens F, Radoshevich L, Cossart P, Ribet D (2014). Mapping of SUMO sites and analysis of SUMOylation changes induced by external stimuli. Proc Natl Acad Sci USA 111, 12432–12437.
Iolascon A, Heimpel H, Wahlin A, Tamary H (2013). Congenital dyserythropoietic anemias: molecular insights and diagnostic approach. Blood 122, 2162–2166.
Jackson B, Peyrollier K, Pedersen E, Basse A, Karlsson R, Wang Z, Lefever T, Ochsenbein AM, Schmidt G, Aktories K, *et al*. (2011). RhoA is dispensable for skin development, but crucial for contraction and directed migration of keratinocytes. Mol Biol Cell 22, 593–605.
Johnson ES, Blobel G (1999). Cell cycle-regulated attachment of the ubiquitin-related protein SUMO to the yeast septins. J Cell Biol 147, 981–994.
Jordan SN, Davies T, Zhuravlev Y, Dumont J, Shirasu-Hiza M, Canman JC (2016). Cortical PAR polarity proteins promote robust cytokinesis during asymmetric cell division. J Cell Biol 212, 39–49.
Kechad A, Jananji S, Ruella Y, Hickson GR (2012). Anillin acts as a bifunctional linker coordinating midbody ring biogenesis during cytokinesis. Curr Biol 22, 197–203.
Kim H, Ding YH, Lu S, Zuo MQ, Tan W, Conte D Jr, Dong MQ, Mello CC (2021). PIE-1 SUMOylation promotes germline fates and piRNA-dependent silencing in C. elegans. Elife 10, e63300.
Kong W, Loison O, Chavadimane Shivakumar P, Chan EH, Saadaoui M, Collinet C, Lenne PF, Clement R (2019). Experimental validation of force inference in epithelia from cell to tissue scale. Sci Rep 9, 14647.
Lacroix B, Letort G, Pitayu L, Salle J, Stefanutti M, Maton G, Ladouceur AM, Canman JC, Maddox PS, Maddox AS, *et al*. (2018). Microtubule dynamics scale with cell size to set spindle length and assembly timing. Dev Cell 45, 496–511.e6.
Lacroix B, Maddox AS (2012). Cytokinesis, ploidy and aneuploidy. J Pathol 226, 338–351.
Lebedev M, Chan FY, Lochner A, Bellessem J, Osorio DS, Rackles E, Mikeladze-Dvali T, Carvalho AX, Zanin E (2023). Anillin forms linear structures and facilitates furrow ingression after septin and formin depletion. Cell Rep 42, 113076.
Lee KY, Green RA, Gutierrez E, Gomez-Cavazos JS, Kolotuev I, Wang S, Desai A, Groisman A, Oegema K (2018). CYK-4 functions independently of its centralspindlin partner ZEN-4 to cellularize oocytes in germline syncytia. Elife 7, e36919.
Lehmann R, Ephrussi A (1994). Germ plasm formation and germ cell determination in Drosophila. Ciba Found Symp 182, 282–296.
Li F, Wang X, Bunger PC, Gerdes AM (1997). Formation of binucleated cardiac myocytes in rat heart: I. Role of actin-myosin contractile ring. J Mol Cell Cardiol 29, 1541–1551.
Li H, Bielas SL, Zaki MS, Ismail S, Farfara D, Um K, Rosti RO, Scott EC, Tu S, Chi NC, *et al*. (2016). Biallelic mutations in citron kinase link mitotic cytokinesis to human primary microcephaly. Am J Hum Genet 99, 501–510.
Li R (2007). Cytokinesis in development and disease: variations on a common theme. Cell Mol Life Sci 64, 3044–3058.
Liljeholm M, Irvine AF, Vikberg AL, Norberg A, Month S, Sandstrom H, Wahlin A, Mishima M, Golovleva I (2013). Congenital dyserythropoietic anemia type III (CDA III) is caused by a mutation in kinesin family member, KIF23. Blood 121, 4791–4799.
Liu J, Maduzia LL, Shirayama M, Mello CC (2010). NMY-2 maintains cellular asymmetry and cell boundaries, and promotes a SRC-dependent asymmetric cell division. Dev Biol 339, 366–373.
Longtine MS, DeMarini DJ, Valencik ML, Al-Awar OS, Fares H, De Virgilio C, Pringle JR (1996). The septins: roles in cytokinesis and other processes. Curr Opin Cell Biol 8, 106–119.
LoTurco JJ, Sarkisian MR, Cosker L, Bai J (2003). Citron kinase is a regulator of mitosis and neurogenic cytokinesis in the neocortical ventricular zone. Cereb Cortex 13, 588–591.
Maddox AS, Habermann B, Desai A, Oegema K (2005). Distinct roles for two C. elegans anillins in the gonad and early embryo. Development 132, 2837–2848.
Maddox AS, Lewellyn L, Desai A, Oegema K (2007). Anillin and the septins promote asymmetric ingression of the cytokinetic furrow. Dev Cell 12, 827–835.
Mango SE, Thorpe CJ, Martin PR, Chamberlain SH, Bowerman B (1994). Two maternal genes, apx-1 and pie-1, are required to distinguish the fates of equivalent blastomeres in the early Caenorhabditis elegans embryo. Development 120, 2305–2315.
Margall-Ducos G, Celton-Morizur S, Couton D, Bregerie O, Desdouets C (2007). Liver tetraploidization is controlled by a new process of incomplete cytokinesis. J Cell Sci 120, 3633–3639.
Marquardt J, Chen X, Bi E (2021). Septin assembly and remodeling at the cell division site during the cell cycle. Front Cell Dev Biol 9, 793920.
Masgrau A, Battola A, Sanmartin T, Pryszcz LP, Gabaldon T, Mendoza M (2017). Distinct roles of the polarity factors Boi1 and Boi2 in the control of exocytosis and abscission in budding yeast. Mol Biol Cell 28, 3082–3094.
Maton G, Edwards F, Lacroix B, Stefanutti M, Laband K, Lieury T, Kim T, Espeut J, Canman JC, Dumont J (2015). Kinetochore components are required for central spindle assembly. Nat Cell Biol 17, 953.
Matsuda K, Jung W, Sato Y, Kobayashi T, Yamagishi M, Kim T, Yajima J. (2024). Myosin-induced F-actin fragmentation facilitates contraction of actin networks. Cytoskeleton.
Mela A, Momany M (2019). Septin mutations and phenotypes in S. cerevisiae. Cytoskeleton 76, 33–44.
Mello CC, Draper BW, Krause M, Weintraub H, Priess JR (1992). The pie-1 and mex-1 genes and maternal control of blastomere identity in early C. elegans embryos. Cell 70, 163–176.
Mello CC, Schubert C, Draper B, Zhang W, Lobel R, Priess JR (1996). The PIE-1 protein and germline specification in C. elegans embryos. Nature 382, 710–712.
Menon MB, Gaestel M (2015). Sep(t)arate or not - how some cells take septin-independent routes through cytokinesis. J Cell Sci 128, 1877–1886.
Menon MB, Sawada A, Chaturvedi A, Mishra P, Schuster-Gossler K, Galla M, Schambach A, Gossler A, Forster R, Heuser M, *et al*. (2014). Genetic deletion of SEPT7 reveals a cell type-specific role of septins in microtubule destabilization for the completion of cytokinesis. PLoS Genet 10, e1004558.
Merritt C, Rasoloson D, Ko D, Seydoux G (2008). 3′ UTRs are the primary regulators of gene expression in the C. elegans germline. Curr Biol 18, 1476–1482.
Morita K, Hirono K, Han M (2005). The Caenorhabditis elegans ect-2 RhoGEF gene regulates cytokinesis and migration of epidermal P cells. EMBO Rep 6, 1163–1168.
Moulding DA, Blundell MP, Spiller DG, White MR, Cory GO, Calle Y, Kempski H, Sinclair J, Ancliff PJ, Kinnon C, *et al*. (2007). Unregulated actin polymerization by WASp causes defects of mitosis and cytokinesis in X-linked neutropenia. J Exp Med 204, 2213–2224.
Munro E, Nance J, Priess JR (2004). Cortical flows powered by asymmetrical contraction transport PAR proteins to establish and maintain anterior-posterior polarity in the early C. elegans embryo. Dev Cell 7, 413–424.
Muzzi P, Camera P, Di Cunto F, Vercelli A (2009). Deletion of the citron kinase gene selectively affects the number and distribution of interneurons in barrelfield cortex. J Comp Neurol 513, 249–264.
Nguyen TQ, Sawa H, Okano H, White JG (2000). The C. elegans septin genes, unc-59 and unc-61, are required for normal postembryonic cytokineses and morphogenesis but have no essential function in embryogenesis. J Cell Sci 113, 3825–3837.
Norden C, Mendoza M, Dobbelaere J, Kotwaliwale CV, Biggins S, Barral Y (2006). The NoCut pathway links completion of cytokinesis to spindle midzone function to prevent chromosome breakage. Cell 125, 85–98.
Oegema K, Savoian MS, Mitchison TJ, Field CM (2000). Functional analysis of a human homologue of the Drosophila actin binding protein anillin suggests a role in cytokinesis. J Cell Biol 150, 539–552.

Ogura K, Kishimoto N, Mitani S, Gengyo-Ando K, Kohara Y (2003). Translational control of maternal glp-1 mRNA by POS-1 and its interacting protein SPN-4 in Caenorhabditis elegans. Development 130, 2495–2503.
Oldenbroek M, Robertson SM, Guven-Ozkan T, Gore S, Nishi Y, Lin R (2012). Multiple RNA-binding proteins function combinatorially to control the soma-restricted expression pattern of the E3 ligase subunit ZIF-1. Dev Biol 363, 388–398.
Paw BH, Davidson AJ, Zhou Y, Li R, Pratt SJ, Lee C, Trede NS, Brownlie A, Donovan A, Liao EC, *et al.* (2003). Cell-specific mitotic defect and dyserythropoiesis associated with erythroid band 3 deficiency. Nat Genet 34, 59–64.
Piekny AJ, Maddox AS (2010). The myriad roles of Anillin during cytokinesis. Semin Cell Dev Biol 21, 881–891.
Qiu R, Runxiang Q, Geng A, Liu J, Xu CW, Menon MB, Gaestel M, Lu Q (2020). SEPT7 interacts with KIF20A and regulates the proliferative state of neural progenitor cells during cortical development. Cereb Cortex 30, 3030–3043.
Rabie EM, Zhang SX, Dunn CE, Nelson CM (2021). Substratum stiffness signals through integrin-linked kinase and beta1-integrin to regulate midbody proteins and abscission during EMT. Mol Biol Cell 32, 1664–1676.
Ravid K, Lu J, Zimmet JM, Jones MR (2002). Roads to polyploidy: the megakaryocyte example. J Cell Physiol 190, 7–20.
Reese KJ, Dunn MA, Waddle JA, Seydoux G (2000). Asymmetric segregation of PIE-1 in C. elegans is mediated by two complementary mechanisms that act through separate PIE-1 protein domains. Mol Cell 6, 445–455.
Rehain-Bell K, Love A, Werner ME, MacLeod I, Yates JR, 3rd, Maddox AS (2017). A sterile 20 family kinase and its co-factor CCM-3 regulate contractile ring proteins on germline intercellular bridges. Curr Biol 27, 860–867.
Ribet D, Boscaini S, Cauvin C, Siguier M, Mostowy S, Echard A, Cossart P (2017). SUMOylation of human septins is critical for septin filament bundling and cytokinesis. J Cell Biol 216, 4041–4052.
Rincon SA, Paoletti A (2012). Mid1/anillin and the spatial regulation of cytokinesis in fission yeast. Cytoskeleton 69, 764–777.
Roelen BAJ, Chuva de Sousa Lopes SM (2022). Stay on the road: from germ cell specification to gonadal colonization in mammals. Philos Trans R Soc Lond B Biol Sci 377, 20210259.
Rose L, Gonczy P (2014). Polarity establishment, asymmetric division and segregation of fate determinants in early C. elegans embryos. WormBook 30, 1–43.
Saga Y (2008). Mouse germ cell development during embryogenesis. Curr Opin Genet Dev 18, 337–341.
Saha S, Pollard TD (2012). Anillin-related protein Mid1p coordinates the assembly of the cytokinetic contractile ring in fission yeast. Mol Biol Cell 23, 3982–3992.
Saitou M (2009). Specification of the germ cell lineage in mice. Front Biosci 14, 1068–1087.
Sallee MD, Zonka JC, Skokan TD, Raftrey BC, Feldman JL (2018). Tissue-specific degradation of essential centrosome components reveals distinct microtubule populations at microtubule organizing centers. PLoS Biol 16, e2005189.
Santos IC, Silva AM, Gassmann R, Carvalho AX (2023). Anillin and the microtubule bundler PRC1 maintain myosin in the contractile ring to ensure completion of cytokinesis. Development 150, dev201637.
Schindelin J, Arganda-Carreras I, Frise E, Kaynig V, Longair M, Pietzsch T, Preibisch S, Rueden C, Saalfeld S, Schmid B, *et al.* (2012). Fiji: an open-source platform for biological-image analysis. Nat Methods 9, 676–682.
Seu KG, Trump LR, Emberesh S, Lorsbach RB, Johnson C, Meznarich J, Underhill HR, Chou ST, Sakthivel H, Nassar NN, *et al.* (2020). VPS4A mutations in humans cause syndromic congenital dyserythropoietic anemia due to cytokinesis and trafficking defects. Am J Hum Genet 107, 1149–1156.
Seydoux G, Dunn MA (1997). Transcriptionally repressed germ cells lack a subpopulation of phosphorylated RNA polymerase II in early embryos of Caenorhabditis elegans and Drosophila melanogaster. Development 124, 2191–2201.
Seydoux G, Mello CC, Pettitt J, Wood WB, Priess JR, Fire A (1996). Repression of gene expression in the embryonic germ lineage of C. elegans. Nature 382, 713–716.
Sgro F, Bianchi FT, Falcone M, Pallavicini G, Gai M, Chiotto AM, Berto GE, Turco E, Chang YJ, Huttner WB, Di Cunto F (2016). Tissue-specific control of midbody microtubule stability by citron kinase through modulation of TUBB3 phosphorylation. Cell Death Differ 23, 801–813.
Shaheen R, Hashem A, Abdel-Salam GM, Al-Fadhli F, Ewida N, Alkuraya FS (2016). Mutations in CIT, encoding citron rho-interacting serine/threonine kinase, cause severe primary microcephaly in humans. Hum Genet 135, 1191–1197.
Shin TH, Mello CC (2003). Chromatin regulation during C. elegans germline development. Curr Opin Genet Dev 13, 455–462.
Sladky VC, Eichin F, Reiberger T, Villunger A (2021). Polyploidy control in hepatic health and disease. J Hepatol 75, 1177–1191.
Straight AF, Field CM, Mitchison TJ (2005). Anillin binds nonmuscle myosin II and regulates the contractile ring. Mol Biol Cell 16, 193–201.
Strome S (2005). Specification of the germ line. WormBook 28, 1–10.
Strome S, Lehmann R (2007). Germ versus soma decisions: lessons from flies and worms. Science 316, 392–393.
Strome S, Updike D (2015). Specifying and protecting germ cell fate. Nat Rev Mol Cell Biol 16, 406–416.
Sulston JE, Schierenberg E, White JG, Thomson JN (1983). The embryonic cell lineage of the nematode Caenorhabditis elegans. Dev Biol 100, 64–119.
Sundaramoorthy S, Garcia Badaracco A, Hirsch SM, Park JH, Davies T, Dumont J, Shirasu-Hiza M, Kummel AC, Canman JC (2017). Low efficiency upconversion nanoparticles for high-resolution coalignment of near-infrared and visible light paths on a light microscope. ACS Appl Mater Interfaces 9, 7929–7940.
Tabara H, Hill RJ, Mello CC, Priess JR, Kohara Y (1999). pos-1 encodes a cytoplasmic zinc-finger protein essential for germline specification in C. elegans. Development 126, 1–11.
Takegahara N, Kim H, Mizuno H, Sakaue-Sawano A, Miyawaki A, Tomura M, Kanagawa O, Ishii M, Choi Y (2016). Involvement of receptor activator of nuclear factor-kappaB ligand (RANKL)-induced incomplete cytokinesis in the polyploidization of osteoclasts. J Biol Chem 291, 3439–3454.
Tamborrini D, Juanes MA, Ibanes S, Rancati G, Piatti S (2018). Recruitment of the mitotic exit network to yeast centrosomes couples septin displacement to actomyosin constriction. Nat Commun 9, 4308.
Tamborrini D, Piatti S (2019). Septin clearance from the division site triggers cytokinesis in budding yeast. Microb Cell 6, 295–298.
Taniguchi K, Kokuryo A, Imano T, Minami R, Nakagoshi H, Adachi-Yamada T (2014). Isoform-specific functions of Mud/NuMA mediate binucleation of Drosophila male accessory gland cells. BMC Dev Biol 14, 46.
Tenenhaus C, Schubert C, Seydoux G (1998). Genetic requirements for PIE-1 localization and inhibition of gene expression in the embryonic germ lineage of Caenorhabditis elegans. Dev Biol 200, 212–224.
Tenenhaus C, Subramaniam K, Dunn MA, Seydoux G (2001). PIE-1 is a bifunctional protein that regulates maternal and zygotic gene expression in the embryonic germ line of Caenorhabditis elegans. Genes Dev 15, 1031–1040.
Timmons L, Court DL, Fire A (2001). Ingestion of bacterially expressed dsRNAs can produce specific and potent genetic interference in Caenorhabditis elegans. Gene 263, 103–112.
Tintori SC, Osborne Nishimura E, Golden P, Lieb JD, Goldstein B (2016). A transcriptional lineage of the early C. elegans embryo. Dev Cell 38, 430–444.
Tormos AM, Talens-Visconti R, Sastre J (2015). Regulation of cytokinesis and its clinical significance. Crit Rev Clin Lab Sci 52, 159–167.
Tsukamoto T, Gearhart MD, Spike CA, Huelgas-Morales G, Mews M, Boag PR, Beilharz TH, Greenstein D (2017). LIN-41 and OMA ribonucleoprotein complexes mediate a translational repression-to-activation switch controlling oocyte meiotic maturation and the oocyte-to-embryo transition in Caenorhabditis elegans. Genetics 206, 2007–2039.
Unhavaithaya Y, Shin TH, Miliaras N, Lee J, Oyama T, Mello CC (2002). MEP-1 and a homolog of the NURD complex component Mi-2 act together to maintain germline-soma distinctions in C. elegans. Cell 111, 991–1002.
Vinciguerra P, Godinho SA, Parmar K, Pellman D, D'Andrea AD (2010). Cytokinesis failure occurs in Fanconi anemia pathway-deficient murine and human bone marrow hematopoietic cells. J Clin Invest 120, 3834–3842.
Wang J, Batourina E, Schneider K, Souza S, Swayne T, Liu C, George CD, Tate T, Dan H, Wiessner G, *et al.* (2018). Polyploid superficial cells that maintain the urothelial barrier are produced via incomplete cytokinesis and endoreplication. Cell Rep 25, 464–477.e4.
Wang JT, Seydoux G (2013). Germ cell specification. Adv Exp Med Biol 757, 17–39.

Wessel GM, Brayboy L, Fresques T, Gustafson EA, Oulhen N, Ramos I, Reich A, Swartz SZ, Yajima M, Zazueta V (2014). The biology of the germ line in echinoderms. Mol Reprod Dev 81, 679–711.
Wontakal SN, Britto M, Zhang H, Han Y, Gao C, Tannenbaum S, Durham BH, Lee MT, An X, Mishima M (2022). RACGAP1 variants in a sporadic case of CDA III implicate the dysfunction of centralspindlin as the basis of the disease. Blood 139, 1413–1418.
Woods BL, Gladfelter AS (2021). The state of the septin cytoskeleton from assembly to function. Curr Opin Cell Biol 68, 105–112.
Wu JQ, Kuhn JR, Kovar DR, Pollard TD (2003). Spatial and temporal pathway for assembly and constriction of the contractile ring in fission yeast cytokinesis. Dev Cell 5, 723–734.
Wu Y, Zhang H, Griffin EE (2015). Coupling between cytoplasmic concentration gradients through local control of protein mobility in the Caenorhabditis elegans zygote. Mol Biol Cell 26, 2963–2970.
Yamamoto K, Ichbiah S, Pinto J, Delbary F, Goehring N, Turlier H, Charras G (2023). Dissecting the subcellular forces sculpting early *C. elegans* embryos. bioRxiv, 2023.2003.2007.531437.
Yoo SK, Deng Q, Cavnar PJ, Wu YI, Hahn KM, Huttenlocher A (2010). Differential regulation of protrusion and polarity by PI3K during neutrophil motility in live zebrafish. Dev Cell 18, 226–236.
Zhang F, Barboric M, Blackwell TK, Peterlin BM (2003). A model of repression: CTD analogs and PIE-1 inhibit transcriptional elongation by P-TEFb. Genes Dev 17, 748–758.